Hydrometeor partitioning ratios for dual-frequency space-borne and polarimetric ground-based radar observations

Velibor Pejcic[1], Kamil Mroz[2], Kai Mühlbauer[1], and Silke Trömel[1,3]

[1]Institute of Geosciences, Department of Meteorology, University of Bonn, Bonn, Germany
[2]National Center for Earth Observation, University of Leicester, Leicester, UK
[3]Laboratory for Clouds and Precipitation Exploration, Geoverbund ABC/J, Bonn, Germany

Correspondence: Velibor Pejcic (velibor@uni-bonn.de)

Abstract. Conventional radar-based hydrometeor classification algorithms identify the dominant hydrometeor type within a resolved radar volume, while newer techniques estimate the proportions of individual hydrometeor classes (hydrometeor partitioning ratios, HPRs) within a mixture. These newer algorithms ($\mathrm{HMC}_{\mathrm{P}}^{\mathrm{DP}}$) are based on dual-polarization measurements from ground-based radars (GR), while to date no comparable algorithms for space-borne radars (SR) with dual-frequency capabilities exist. This study (1) further improves HPR estimates based on GR dual-polarization measurements, (2) exploits the combination of dual-frequency SR and dual-polarization GR to introduce HPRs based on dual-frequency observations only, and (3) evaluates GR- and SR-based HPR retrievals. To achieve these objectives, dual-polarization measurements of NEXRAD's GRs are matched with those of the dual-frequency precipitation radar of the Global Precipitation Measurement Core satellite. All matched volumes are represented by averaged dual-frequency and dual-polarization observations and several hundred GR sub-volumes classified with standard hydrometeor classification. The latter are used to calculate quasi-HPRs (qHPRs). qHPRs and averaged dual-frequency and dual-polarization variables of the training dataset are used to derive covariances and centroids for each hydrometeor class. They serve as the basis for dual-frequency and dual-polarization based HPR retrievals within $\mathrm{HMC}_{\mathrm{P}}$ and are applied to the test dataset. The ensuing evaluation of HPR retrievals is performed with the qHPRs of the test dataset. HPRs show for most hydrometeor classes high correlations with the qHPRs and confirm the overall good $\mathrm{HMC}_{\mathrm{P}}$ performance. However, dual-polarization based classification performance is superior to dual-frequency ones. Both underestimate snow, overestimate graupel, and result in low correlations for big drops.

1 Introduction

Hydrometeor classifications (HMC) using ground-based polarimetric weather radars (GR) observations play an essential role, e.g. to refine quantitative precipitation estimation (Giangrande and Ryzhkov, 2008; Chen et al., 2017; Cifelli et al., 2011), to detect hail and estimate its size and damage potential (Ortega et al., 2016; Ryzhkov et al., 2013; Ackermann et al., 2023) and to identify freezing rain (Thompson et al., 2014), which can serve as a warning system for transport infrastructure (Trömel et al., 2017). The majority of HMCs identify the dominant hydrometeor type within each resolved radar volume exploiting measurements from dual-polarization (DP) weather radars and specific classification methods. The most commonly used classification methods are based on the fuzzy logic approach (Dolan and Rutledge, 2009; Dolan et al., 2013; Zrnić et al., 2001a;

Straka et al., 2000; Thompson et al., 2014; Ribaud et al., 2016; Park et al., 2009), but there are also methods that rely on the Bayesian approach (Yang et al., 2019; Marzano et al., 2007) or clustering techniques (Grazioli et al., 2015; Ribaud et al., 2019; Lukach et al., 2020; Besic et al., 2016). More detailed description of hydrometeor mixtures (Besic et al., 2018) are the so-called hydrometeor partitioning ratios (HPRs), which represent estimates of the proportion of the polarimetric signal originating from a specific hydrometeor class within a resolved radar volume. Besic et al. (2018) provided a methodology to estimate HPRs, which was subsequently refined in Trömel et al. (2023). HPRs have recently been utilized to study microphysics and dynamics of precipitation (Gehring et al., 2020, 2022), to verify microphysical retrievals (Billault-Roux et al., 2023; Planat et al., 2021) and to evaluate hydrometeor distributions in NWP models (Trömel et al., 2021; Vignon et al., 2019; Jang et al., 2021; Shrestha et al., 2022; Trömel et al., 2023).

Only a few space-borne measurement platforms with radars exist or have existed in the past: CloudSat (Stephens et al., 2002), designed for observations of clouds and light precipitation, the Tropical Rainfall Measuring Mission (TRMM; Liu et al., 2012), which is the first precipitation satellite with a Ku-band precipitation radar (PR) on board, and its successor the Global Precipitation Measurement core satellite (GPM) with the first Dual-Frequency Precipitation Radar (DPR) measuring precipitation at Ku-band and Ka-band frequencies (Hou et al., 2014). Rain rates estimated from space-borne radars (SR) are significantly affected by the hydrometeor types located within a resolved measurement volume (Liao and Meneghini, 2022). SR-derived HMCs, using the DPR e.g., are based on very simple subdivisions of the hydrometeors. The detection of the melting layer (ML) top and bottom is used to distinguish between solid, liquid and melting hydrometeors (Le et al., 2016). Additional two-dimensional classifications are provided for snow (*flagSurfaceSnowfall;* Le et al., 2017)), graupel/hail (*flagGraupelHail;* Le and Chandrasekar, 2021a) and hail (*flagHail;* Le and Chandrasekar, 2021b) and are based on the so-called precipitation type index (PTI). The PTI is derived from the storm top height (STH), the maximum measured reflectivity at Ku-band and the average slope of the dual-frequency ratio profile. Mroz et al. (2017) presented several hail detection algorithms based on DF profile observations but also on brightness temperature measurements of GPMs Microwave Imager (GMI). All products do not provide information on the vertical distribution of these hydrometeor classes and are not considered in DPRs rain rates estimation (Iguchi et al., 2010). Seiki (2021) was the first to develop a three-dimensional HMC based on dual-frequency (DF) measurements, but only for hail detection.

In this study, the HMC scheme from Trömel et al. (2023) ($\mathrm{HMC_P}$; introduced by (Pejcic et al., 2021)), estimating HPRs in DP-space ($\mathrm{HMC_P^{DP}}$), is refined and extended to the DF-space ($\mathrm{HMC_P^{DF}}$). For this purpose, satellite-based DF observations from GPM's DPR are combined with ground-based DP measurements from NEXRAD's S-band WSR-88D radars. In order to combine the high-resolution GR and the low-resolution SR data, the DF and DP measurements are averaged to obtain data with approximately equal volumes, so-called superobbed data. Each superobbed observation then contains information about the partitioning ratios of the different dominant hydrometeor classes (quasi hydrometeor partitioning ratio, qHPR), approximated by the relative occurrences of the dominant hydrometeor classes in high-resolution radar bins within the supperobbed volume as determined by conventional DP-based HMC. These qHPRs are used as a basis for the derivation of the HPRs in DF and DP space. Subsequently, the HPRs estimated with $\mathrm{HMC_P}$ from either superobbed DF or DP measurements are validated using the qHPR estimates.

Sect. 2 introduces the SR and GR measurements and their processing, followed by the explanations of the merging procedure and the qHPR derivation. Sect. 3 explains the methodology for HPR estimates. The results are shown in Sect. 4 followed by a conclusion in Sect. 5. All abbreviations can be found in Tab. C.

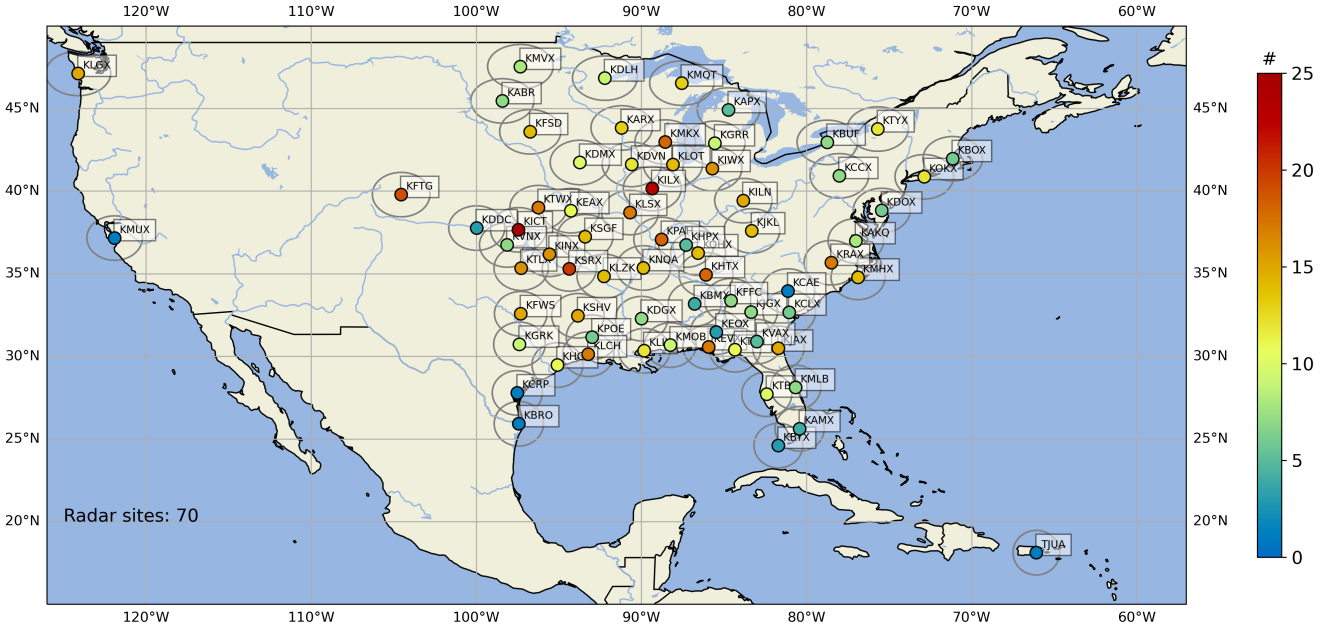

Figure 1. NEXRAD weather radar (WSR-88D) sites provided and quality controlled by the GPM-GV and exploited in this study. The 150 km range for an elevation angle of 0.5° is illustrated as gray circle. The colored dots indicate the location of the respective radar and the number of GPM overpasses in the period between 2014 and 2023 used in this study. The total number of used radar sites is indicated in the lower left corner.

2 Data

2.1 Space-borne radar observations

The DPR onboard the GPM Core Observatory (Iguchi and Meneghini, 2021) comprises two radars: the Ku-band Precipitation Radar (KuPR, 13.6 GHz) and the Ka-band Precipitation Radar (KaPR, 35.5 GHz). The DPR provides measurements with a

vertical resolution of 250 m, over-sampled every 125 m, and a horizontal resolution of approximately 5 km due to the satellite's altitude of 407 km before the orbit boost in November 2023 (Kubota et al., 2024).

Initially, the KuPR operated across a 245 km wide swath (49 beams), while the KaPR was limited to a narrower central swath of 125 km (25 beams), nested within the KuPR swath. The KaPR employed two distinct scanning modes: Measurements with a vertical resolution of 250 m, fully overlapping the central part of the KuPR swath (High-Resolution Mode). Measurements with a vertical resolution of 500 m, where the scan pattern was laterally shifted by half a footprint (24 beams) in the cross-track direction (Shifted Scan Mode, Hou et al., 2014).

On 21 May 2018, the scanning strategy was updated to extend the KaPR swath to 245 km, matching the KuPR swath width. The 24 beams were moved to the outer parts of the swath. This adjustment ensured that all footprints in the extended KaPR swath included DF measurements, significantly enhancing data consistency and coverage (Iguchi et al., 2010). Single-frequency beams are not considered in this study. To derive parameters of the drop size distribution, precipitation rates and attenuation corrected Ku-band and Ka-band reflectivities in logarithmic space, the measured Ka-band (Z^{m}_{Ka}) and Ku-band (Z^{m}_{Ku}) reflectivities are processed in various modules described in more detail in Iguchi et al. (2010). The DF ratio

$$DFR = Z^{m}_{Ku} - Z^{m}_{Ka} \quad (1)$$

is the difference between Z^{m}_{Ku} and Z^{m}_{Ka} reflectivities in logarithmic space. In stratiform precipitation DFR is mainly affected by non-Rayleigh scattering effects and path-integrated attenuation. In the solid phase, attenuation by frozen hydrometeors is negligible for both frequencies and does not significantly change DFR. In contrast, the non-Rayleigh scattering effects play a major role and lead to an increase of the DFR with increasing hydrometeor diameters (Le et al., 2016; Iguchi et al., 2018). Also, DFR in the solid region depends on the density of hydrometeors and their degree of riming. According to the Mie theory an increase in DFR is expected with decreasing density of fluffy non-rimed solid hydrometeors with low Z^{m}_{Ku} (Seiki, 2021). For a fixed DFR Z^{m}_{Ku} increases with the ice particles degree of riming. However, this is only valid in stratiform precipitation and if DFR>1 dB (Tridon et al., 2019). In the melting layer (ML) we observe an increase in Z^{m}_{Ku} due to the changes in the refractive index, particle size and concentration (Ryzhkov and Zrnic, 2019). As a consequence, both non-Rayleigh scattering effects and attenuation increase the DFR and result in a pronounced "bump", called the DFR bright band, in the vertical profile of the DFR (Le et al., 2016). In the liquid phase, attenuation mainly controls the DFR. Ka-band measurements are much more affected by attenuation compared to measurements at Ku-band and lead to an increase in DFR towards the ground. This increase is even more pronounced in convective precipitation where higher precipitation rates, thus the attenuation values, are observed. Furthermore, convection promotes the presence of large hydrometeors such as graupel, hail or drop diameter exceeding 0.8 mm (Mroz et al., 2024) that contribute to non-Rayleigh related DFR increase. In deep convective cores, the typical vertical profile of DFR can be distorted by multiple scattering at Ka-band . In extreme multi-scattering conditions, attenuation of the high frequency radar observations is compensated by multiple scattering effects in the upper part of the atmosphere which results in the so-called DFR-knee, i.e. a decrease in DFR towards the ground (Battaglia et al., 2014).

The overall vertical structure of the DFR is used to categorize the measurements into different rain types (RT, stratiform, convective, other, see Le et al. (2016)) and to determine the ML thickness and height, and is used to distinguish between liquid, solid and melting precipitation regions (Iguchi et al., 2010; Le and Chandrasekar, 2012).

2.2 Ground-based radar observations

DP measurements of the NEXRAD WSR-88D S-band weather radars are exploited for this study. In total, 757 volume scans measured between 2014 and 2023 of the radar sites shown in Fig. 1 are considered. Measurements were selected to ensure that the GPM overflight took place at the closest point in time. A balanced number of convective and stratiform events is maintained to ensure a good representation of less frequently occurring hydrometeors like hail. The range resolution of the utilized NEXRAD radars is 250 m with a maximum elevation angle of 19.5° and 1° degree azimuthal resolution for higher elevation. Only quality-controlled GR observations provided by NASA's GPM Ground Validation program (GPM-GV) are used. The eastern GR sites of the NEXRAD network are predominantly used in the GPM-GV. GPM-GVs quality control includes the removal of non-precipitating echoes with different thresholds and phase unfolding. In addition, GPM-GV also provides vertical temperature information from model soundings (Pippitt et al., 2013).

The vertical temperature profiles are interpolated linearly at the beam center ($\mathrm{T_c}$) and at the respective outer beam edges (3 dB beam width). From now on referred to $\mathrm{T_t}$ as temperature at the top beam edge and $\mathrm{T_b}$ as the temperature at the bottom beam edge. All radar bins with $\mathrm{T_b}$<0°C are classified as solid and all those with $\mathrm{T_t}$>4°C as liquid. All other radar measurements are considered as partly melted. Additional GR processing e.g. phase processing, GR calibration and attenuation correction are explained in more detail in the appendix A.

The applied standard HMC ($\mathrm{HMC_Z}$; Zrnić et al., 2001b) to identify the dominant hydrometeor type in a resolved radar volume and used to estimate the qHPRs is based on two dimensional membership functions (MSF) defined in Park et al. (2009) with slightly modified hydrometeor types and MSF-parameters. The predefined hydrometeor types are light rain, moderate rain, heavy rain, big drops, rain/hail, graupel, crystals, dry snow, wet snow, plates/dendrites and hail. The hydrometeor classes are generally abbreviated to $\mathrm{HM_k}$ where $k = 1, \ldots,$ n with n=11. For more information on $\mathrm{HMC_Z}$, we refer to the appendix B .

2.3 GR-SR Merging

The volume matching method (VMM) is performed with ωradlib (Heistermann et al., 2013) and represents a well-known method for transferring SR and GR measurements to comparably sized volumes. In a first step all DP measurements of all GR bins within the SR footprint are averaged ($\overline{\mathrm{DP}}$, Fig. 2, left, plan view). Secondly, the DF observations of all SR bins (vertical resolution 125 m) within the GR beamwidth are averaged ($\overline{\mathrm{DF}}$, Fig. 2, right, side view). For more details see Warren et al. (2018) or Pejcic et al. (2022). This results in equally sized superobbed volumes described by averaged DP variables $\overline{\mathrm{Z}}_\mathrm{H}$, $\overline{\mathrm{Z}}_\mathrm{DR}$, $\overline{\mathrm{K}}_\mathrm{DP}$ and $\overline{\rho}_\mathrm{HV}$ and averaged DF variables $\overline{\mathrm{Z}}^\mathrm{m}_\mathrm{Ku}$, $\overline{\mathrm{Z}}^\mathrm{m}_\mathrm{Ka}$ and $\overline{\mathrm{DFR}}$, from now on called sample $\mathrm{S_i}$ (Fig. 2, top center and Fig. A1, blue box). Furthermore, each $\mathrm{S_i}$ contains a mean temperature ($\overline{\mathrm{T}}$) and a rain type index ($\overline{\mathrm{RT}}$). $\overline{\mathrm{RT}}$ is convective if more then 10% of the GR pixels in a $\mathrm{S_i}$ are defined as convective ($\overline{\mathrm{RT}} = 2$), otherwise $\overline{\mathrm{RT}}$ is defined as stratiform ($\overline{\mathrm{RT}} = 1$). $\mathrm{S_i}$ also

includes the number of dominant hydrometeor classes $\mathrm{N(HM_k)}$ classified with $\mathrm{HMC_Z}$ on the original GR radar grid (Fig. A1, blue box). For each $\mathrm{S_i}$ the $\mathrm{N(HM_k)}$ are used to calculate the $\mathrm{qHPR_k}$ via

$$qHPR_k = \frac{N(HM_k)}{\sum_{k=0}^{n} N(HM_k)}. \tag{2}$$

Note that qHPRs only represent estimators for the HPRs. E.g., due to their disproportionate influence on the polarimetric moments, hail or graupel may be classified as the dominant hydrometeor class in radar volumes despite low HPR. This can lead to overestimated qHPR for graupel and hail. In this study only $\mathrm{S_i}$ with at least 50 valid GR pixels, well-defined stratiform or convective SR profiles and DPR detected precipitation (*flagPrecip*) are considered. $\mathrm{S_i}$ showing strong differential attenuation due to hot spots above the ML or depolarization streaks (Ryzhkov and Zrnic, 2019) leading to negative $\mathrm{Z_{DR}}$ stripes are excluded. Furthermore, SR observations below 15.5 dBZ at Ku-band (Liao and Meneghini, 2022) and 18 dBZ at Ka-band (Mroz et al., 2024) are not considered.

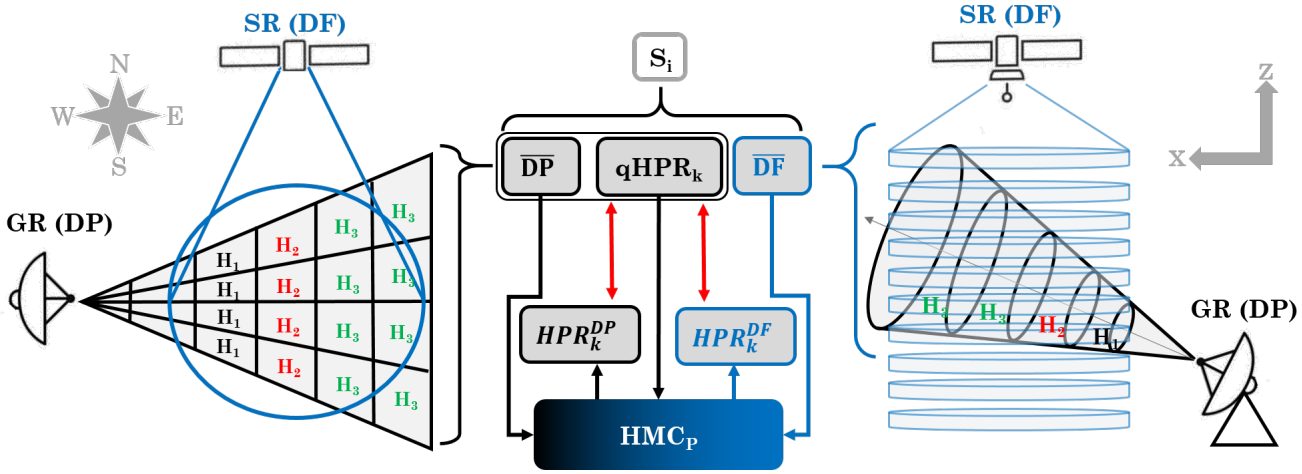

Figure 2. Schematic illustration of the workflow to derive and evaluate the HPR with $\mathrm{HMC_P}$ based on $\overline{\mathrm{DF}}$, $\overline{\mathrm{DP}}$ and $\mathrm{qHPR_k}$ (center) by comparing SR (in blue) and GR (in black) observations. The plan view on the left and the side view on the right site. The hydrometeor classes are indicated with colored H_1, H_2 and H_3

80% of the $\mathrm{S_i}$, including $\overline{\mathrm{DF}}$, $\overline{\mathrm{DP}}$ measurements and qHPRs, serve as training data for the $\mathrm{HMC_P}$ (Fig. 2, center) and the remaining 20% of the $\mathrm{S_i}$ are utilized as test dataset for the evaluation. Sect. 4.1 presents results for one case study entirely independent of the test and training dataset used.

3 Hydrometeor partitioning Ratios (HPR)

In the following, we interpret the polarimetric measurements as multidimensional vectors and thus assume HPRs can be determined based on multidimensional distribution functions p_k for the different hydrometeor classes. If the multidimensional measurement approaches the mean of a specific p_k, the $\mathrm{HPR_k}$ for that particular hydrometeor class k, increases, and vice versa, the farther away it is, the smaller the $\mathrm{HPR_k}$ becomes (Besic et al., 2018; Trömel et al., 2023). Trömel et al. (2023) introduced $\mathrm{HMC_P}$ as a modified version compared to Besic et al. (2018). This section details further advancements of $\mathrm{HMC_P}$ and additionally transfers the methodology from DP to DF observation space.

The supperobbed variables in samples $\mathrm{S_i}$ are stored in the multidimensional observation vector

$$\boldsymbol{X_i}^{DP} = \begin{bmatrix} \overline{Z}_H \\ \overline{Z}_{DR} \\ \overline{K}_{DP} \\ \overline{\rho}_{HV} \\ \overline{RT} \end{bmatrix} \tag{3}$$

including the averaged DP variables $\overline{\mathrm{Z}}_\mathrm{H}$, $\overline{\mathrm{Z}}_\mathrm{DR}$, $\overline{\mathrm{K}}_\mathrm{DP}$ and $\overline{\rho}_\mathrm{HV}$, together with the rain type index $\overline{\mathrm{RT}}$. Similarly, the multidimensional DF observation vector

$$\boldsymbol{X_i}^{DF} = \begin{bmatrix} \overline{Z}^m_{Ku} \\ \overline{DFR}^m_{Ku-Ka} \\ \overline{RT} \end{bmatrix} \tag{4}$$

includes the averaged DF variables $\overline{\mathrm{Z}}^\mathrm{m}_\mathrm{Ku}$and $\overline{\mathrm{DFR}}$, together with $\overline{\mathrm{RT}}$. The ensuring description of the algorithm refers to an observation vector $\boldsymbol{X_i}$ and is valid for both multidimensional vectors $\boldsymbol{X}^\mathrm{DF}_\mathrm{i}$ and $\boldsymbol{X}^\mathrm{DP}_\mathrm{i}$.

In order to derive p_k, weighted centroids

$$\boldsymbol{\mu}_\mathrm{k} = \frac{\sum_{i=1}^{n} w_i \boldsymbol{X_i}}{\sum_{i=1}^{n} w_i} \tag{5}$$

and weighted covariance matrices

$$\boldsymbol{C}_\mathrm{k} = \frac{\sum_{i=1}^{n} w_i \left((\boldsymbol{X_i} - \boldsymbol{\mu_k})(\mathbf{X_i} - \boldsymbol{\mu_k})^\top \right)}{\sum_{i=1}^{n} w_i} \tag{6}$$

are calculated with the weighting factors w_i= $\mathrm{qHPR_k}$ based on all available $\mathrm{S_i}$ for each hydrometeor class k in DP and DF space. Besic et al. (2016) and Trömel et al. (2023) apply a clustering algorithms to the multidimensional DP measurements and identified clusters are then assigned to specific hydrometeor classes using state-of-the-art HMC. Centroids $\boldsymbol{\mu}_k$ (in Trömel et al. (2023) also $\boldsymbol{C}_k$) are then calculated for these clusters. However, non-physical clusters in terms of precipitation microphysics and strict boundaries between clustered data may arise, which have an impact on the calculations of centroids and covariance matrices in polarimetric space. Instead, the use of qHPR as weighting factors enables a more physical transition between the

DP or DF variables for different hydrometeor classes. The multidimensional distribution functions p_k are calculated based on centroids $\boldsymbol{\mu}_k$ and covariances $\boldsymbol{C}_k$ (Eq.5 and Eq.6) assuming a multivariate normal distribution

$$p_k(\boldsymbol{X}|\boldsymbol{\mu_k},\boldsymbol{C_k}) = \Lambda \exp\left(-\frac{1}{2}(\boldsymbol{X}-\boldsymbol{\mu_k})^{\mathsf{T}}\boldsymbol{C_k}^{-1}(\boldsymbol{X}-\boldsymbol{\mu_k})\right) \tag{7}$$

with the transpose of a matrix $(\cdot)^{\mathsf{T}}$, the dimension d of the multivariate normal distribution and $\Lambda = 1/\sqrt{(2\pi)^d|\boldsymbol{C_k}|}$, where $|\cdot|$ denotes the the determinant (Trömel et al., 2023). The multivariate normal distribution p_k replaces the exponential distribution used in Besic et al. (2018), allowing a more suitable elliptical (instead of only spherical) distributions of DP or DF variables for different hydrometeor classes. Besic et al. (2018) use the entropy to determine the shape of p_k, which is a purely statistical method. The inherent assumption is that the entropy and thus the mixing is highest exactly between two centroids. Trömel et al. (2023) describe the shape of p_k with the observed distribution of the DP measurements in multidimensional space using the covariance matrices. Including now the qHPRs, as weighted factors, the centroids and covariance matrices are no longer restricted to the clusters with strict boundaries in polarimetric space, instead overlapping distributions are enabled.

The value of a $\mathrm{p_k}(\boldsymbol{\mu_k})$ equals 1 according for an unmixed observation (Besic et al., 2018), of only one specific hydrometeor class. Therefore, each $p_k(\boldsymbol{X})$ is normalized with $p_k(\boldsymbol{\mu_k})$:

$$\tilde{p}_k = \frac{p_k(\boldsymbol{X})}{p_k(\boldsymbol{\mu_k})}. \tag{8}$$

Finally, HPRs for different hydrometeor classes k are estimated as follows:

$$\mathrm{HPR}_k = \frac{W_k(T)\,\tilde{p}_k}{\sum_{k=1}^{n} W_k(T)\,\tilde{p}_k}. \tag{9}$$

The weighting functions $\mathrm{W_k(T)}$ suppress HPR estimates of hydrometeor classes in unexpected temperature regions. $\mathrm{W_k(T)}$ are derived from statistics of the relative occurrence of the different hydrometeor classes ($\mathrm{N(HM_k)}$) in 2°C intervals between -80°C and 32°C. Resulting estimates of partitioning ratios for different hydrometeor classes k are referred to as $\mathrm{HPR_k^{DP}}$ and $\mathrm{HPR_k^{DF}}$ in DP and DF space, respectively.

4 Results

4.1 Multidimensional distribution function p_k in polarimetric and dual-frequency space

The $\tilde{p}_k$ of the DP (Fig. 3) and DF variables (Fig. 4d, e and f), as well as of RT (Fig. 4a, b and c) for each hydrometeor class k are derived based on the training data set (Fig. 2, center) as described in Sect. 3 and represent the basis for the $\mathrm{HMC_P}$. The hydrometeor classes are analyzed separately in the regions where they are most likely to occur, e.g. light rain, moderate rain, heavy rain and big drops in the liquid region, plates/dendrites, ice crystals and snow in the solid region and wet snow, graupel, hail and rain/hail in the solid, liquid and melting region (mixed). Note that the figures mentioned above illustrate only two-dimensional representations of the multidimensional $\tilde{p}_k$, normalized according to Eq. 8 without weighting $W_k(T)$.

In DP space, the centroids of the hydrometeor classes light rain, moderate rain, heavy rain (Fig. 3a, d and g) show in the Z_H-Z_{DR} and Z_H-K_{DP} plane an increasing Z_H with increasing Z_{DR} and K_{DP} respectively . With increasing Z_H ρ_{HV} is decreasing due to droplet growth and the associated increase in droplet flattening in liquid precipitation (Straka et al., 2000). The big drops centroid shows an increased Z_{DR} compared to light rain, moderate rain, heavy rain (Bechini and Chandrasekar, 2015). In DP space of the solid region (Fig. 3b, e and h), the centroids of plates/dendrites differ from crystals with respect to high Z_{DR} and K_{DP} values, which is in line with expected characteristics of ice particles especially in the dendritic growth layer (DGL). Dry snow instead is characterized by reduced Z_{DR} and K_{DP} values but higher Z_H values, which is due to the increase in particle size and decrease in density during aggregation processes. As expected the $\tilde{p}_k$ for plates/dendrites show reduced ρ_{HV} values due to the diversity of ice particles in the DGL (Trömel et al., 2019; Thompson et al., 2014). With regard to the mixed hydrometeors (Fig. 3c, f and i) Z_H of the wet snow centroid is much lower compared to the ones of graupel, rain/hail and hail. The latter shows the highest Z_H. ρ_{HV} is the lowest in wet snow, followed by the two hail classes and then graupel. Hail and graupel show lower Z_{DR} values compared to rain/hail and wet snow due the impact of tumbling of hail and potentially conical shapes of graupel (Straka et al., 2000).

In DF space (only Z^m_{Ku}-DFRspace is shown) the centroids for liquid hydrometeors (Fig. 4d) show the typical behavior with increasing DFR and increasing Z^m_{Ku} due to increasing attenuation effects transitioning from light rain to heavy rain (Le and Chandrasekar, 2012). An even more pronounced increase in DFR with rising Z^m_{Ku} is observed for big drops. This can be attributed to the additional influence of non-Rayleigh scattering effects when the droplet diameter exceeds 0.8 mm (Mroz et al., 2024). DFR show an increase for both crystals and snow with increasing Z^m_{Ku} due to the increasing impact of non-Rayleigh effects with increasing particle diameter (Fig. 4e). Graupel, wet snow and rain/hail (Fig. 4f) show increased DFR due to a combination of increased diameters, riming and attenuation effects (Le and Chandrasekar, 2021a; Tridon et al., 2019). Note that DF variables do not significantly differ between rain/hail and hail nor between crystals and plates/dendrites (not shown). As a consequence the hydrometeor classes are merged to rain/hail and crystals.

Big drops, graupel, rain/hail and hail are mostly restricted to convective precipitation where heavy rain has higher tendency to appear also in stratiform precipitation. Light rain, wet snow, dry snow, crystals and plates/dendrites are restricted to stratiform precipitation where wet snow, dry snow, crystals and plates/dendrites can occur with lower probabilities also in convection (Fig. 4a, b and c).

4.2 Evaluation with quasi hydrometeor partitioning ratios

In order to evaluate the DF- and DP-based HPR retrievals, HMC_P estimates (E) of the test dataset are compared to the qHPR serving as the reference (R), with the following statistical metrics:

$$\mathrm{BIAS} = \sqrt{\frac{1}{N}\sum_{i=1}^{N}(E_i - R_i)} \quad , \tag{10}$$

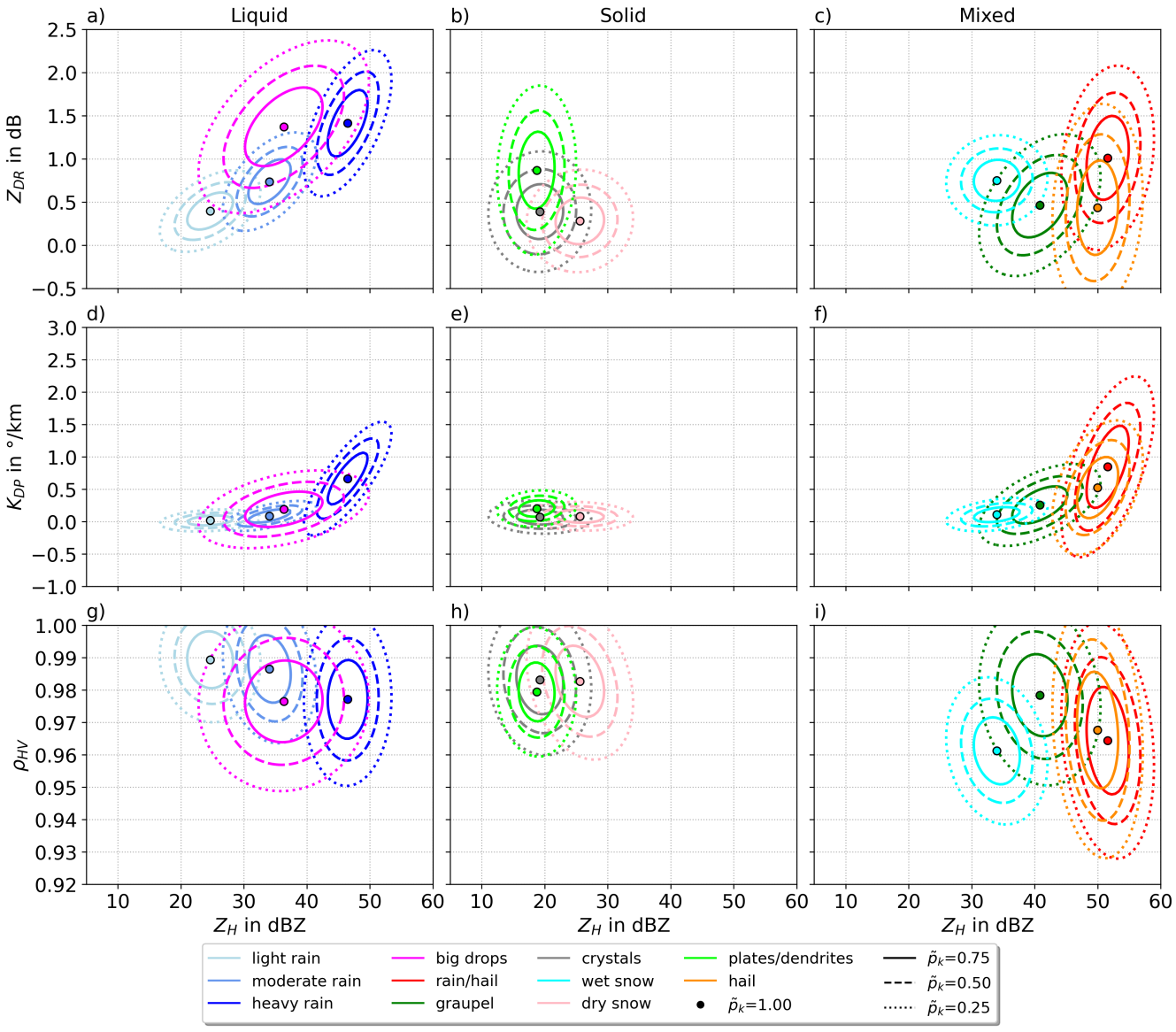

Figure 3. Normalized probability density functions $\tilde{p}_k$ of the DP variables Z_H against Z_{DR} (a, b, and c), Z_H against K_{DP} (d, e and f) and Z_H against ρ_{HV} (g, h and i) for liquid hydrometeors (light rain, moderate rain, heavy rain and big drops, left column), solid hydrometeors (plates/dendrites, dry snow, crystals, center column) and mixed phase hydrometeors (rain/hail, wet snow, graupel and hail, right column). The different contour lines indicating the probabilities of the given $\tilde{p}_k$ for the different hydrometeor classes.

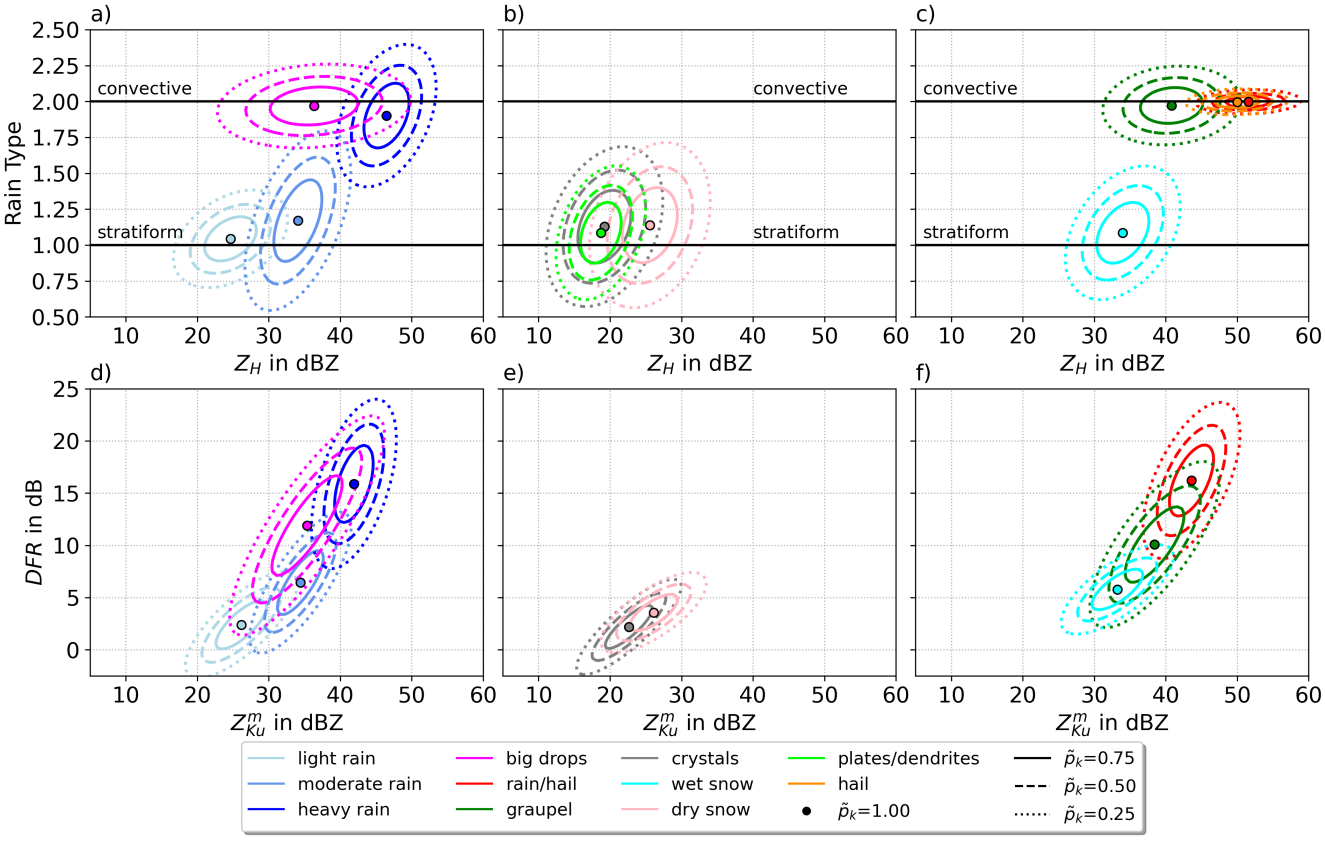

Figure 4. Normalized probability density function $\tilde{p}_k$ of $\mathrm{Z_H}$ in relation to the RT (a, b and c) and the DF variables ($\mathrm{Z^m_{Ku}}$ in relation to DFR, d, e and f), for liquid hydrometeors (light rain, moderate rain, heavy rain and big drops, left column), solid hydrometeors (plates/dendrites, dry snow, crystals, center column) and mixed phase hydrometeors (rain/hail, wet snow, graupel and hail, right column). The different contour lines indicating the probabilities of the given $\tilde{p}_k$ for the different hydrometeor classes.

$$\mathrm{RMSE} = \sqrt{\frac{1}{N}\sum_{i=1}^{N}\left(E_i - R_i\right)^2} \text{ and} \tag{11}$$

$$\mathrm{CCP} = \frac{\sum_{i=1}^{N}\left(E_i - \overline{E}\right)\left(R_i - \overline{R}\right)}{\sqrt{\sum_{i=1}^{N}\left(E_i - \overline{E}\right)^2 \sum_{i=1}^{N}\left(R_i - \overline{R}\right)^2}}. \tag{12}$$

$\overline{\mathrm{R}}$ and $\overline{\mathrm{E}}$ denote the mean values of $\mathrm{R_i}$ and $\mathrm{E_i}$, respectively. A comparison between the qHPRs and HPRs based on the $\overline{\mathrm{DF}}$ and $\overline{\mathrm{DP}}$ variables results in high CCP for several hydrometeor classes. E.g., CCPs higher than 0.8, are achieved with the DP-based retrievals for light rain, moderate rain, heavy rain, wet snow, crystals and dry snow and with the DF-based retrievals

for light rain, moderate rain, and dry snow (Fig. 5a, b, c, d, e, o, m, q and r). The lowest correlations occur with $\mathrm{HPR}_{\mathrm{k}}^{\mathrm{DP}}$ and $\mathrm{HPR}_{\mathrm{k}}^{\mathrm{DF}}$ of big drops (Fig. 5g and h) followed by $\mathrm{HPR}_{\mathrm{k}}^{\mathrm{DF}}$ of rain/hail and crystals and $\mathrm{HPR}_{\mathrm{k}}^{\mathrm{DP}}$ of plates/dendrites (Fig. 5j, n and t). The largest underestimations can be found in snow in both the DP and DF space, with a BIAS up to -5.15% (Fig.5, q and r) followed the $\mathrm{HPR}_{\mathrm{k}}^{\mathrm{DP}}$ of light rain and moderate rain and $\mathrm{HPR}_{\mathrm{k}}^{\mathrm{DF}}$ of crystals and wet snow (Fig.5, a, c, n and p). Pronounced HPR overestimation occurs for heavy rain, graupel for DF- and DP-based retrievals as well as for $\mathrm{HPR}_{\mathrm{k}}^{\mathrm{DP}}$ of big drops (Fig. 5e, f, g, k, and l). The comparison of hail HPRs shows an overestimation of rain/hail and hail $\mathrm{HPR}_{\mathrm{k}}^{\mathrm{DP}}$ and small underestimation of $\mathrm{HPR}_{\mathrm{k}}^{\mathrm{DF}}$ of rain/hail (Fig. 5i, j and s). Note that qHPR estimated from the dominant hydrometeor classes may overestimate the actual partitioning ratios due to the disproportional impact of hail on DP variables. As a consequence the biases in $\mathrm{HPR}_{\mathrm{k}}^{\mathrm{DP}}$ of rain/hail and hail may be even more pronounced than indicated by the qHPR-based evaluation. BIAS and RMSE values are small for the hail classes and big drops, which can be attributed to their overall low HPR values.

In summary the DP-based retrievals outperform the ones based on DF in terms of CCP and RMSE, in most cases also with respect to the BIAS values. This can be attributed to the higher information content of DP compared to DF measurements, for example, regarding the shape, orientation and homogeneity of the hydrometeors within the measurement volume. Except for the big drops estimates, the retrievals for liquid hydrometeors in both DF- and DP-space, achieve a higher accuracy compared to the retrievals for the solid hydrometeor classes, reflecting the increased complexity and variability of DP and DF signals for solid and mixed hydrometeors.

4.3 Case study

To verify and illustrate the plausibility of the $\mathrm{HMC_P}$ retrievals, a GPM overflight is directly compared to the KDDC NEXRAD GR and a pseudo range height indicator (RHI) is generated along DPRs along-track scan (Fig. 6a, blue dashed and red solid lines). The DP (Fig. 6b, d, f and h) and DF (Fig. 6c, e and g) variables are exploited to derive and compare the $\mathrm{HPR}_{\mathrm{k}}^{\mathrm{DP}}$(Fig. 8) and $\mathrm{HPR}_{\mathrm{k}}^{\mathrm{DF}}$(Fig. 7) with the $\mathrm{HMC_P}$.

A comparison of the GR and SR measurements (Fig. 6) reveals a slight discrepancy in the STH. While GR measurements indicate a STH of approximately 15 km, SR indicate lower values due to the KuPR and KaPR sensitivity (Iguchi et al., 2010). The precipitation event can be subdivided into a stratiform and convective region. According to the GR-based RT classification, the convective area starts at a distance of 60 km from the GR, while the SR classification indicates that the convective area starts at a distance of 50 km. This discrepancy is likely attributable to the presence of a bright band located approximately at 3.5 km height characterized by increased $\mathrm{Z_H}$, $\mathrm{Z_{DR}}$, and reduced ρ_{HV} values, which is not properly identified by the DPR between 50 km and 60 km range and thus partly classified as a convective region. Additionally, the GR has identified further convective areas up to a distance of 40 km, which may not be detected by SR due to their relatively small scale. The GR beams of higher elevation angles are affected by differential attenuation in the ML resulting in negative $\mathrm{Z_{DR}}$ (Fig. 6d). At distances of approximately 80 km and beyond, the measurements at low elevation angles are partially affected by non-uniform beam filling (NBF), characterized by extreme high ϕ_{DP} (not shown) and low ρ_{HV} values (Ryzhkov and Zrnic, 2019). In the convective region, the impact of attenuation on SR near surface measurements is significant, especially at Ka-band (not shown). The signal partially drops below the 18 dBZ Ka-band threshold and is therefore excluded.

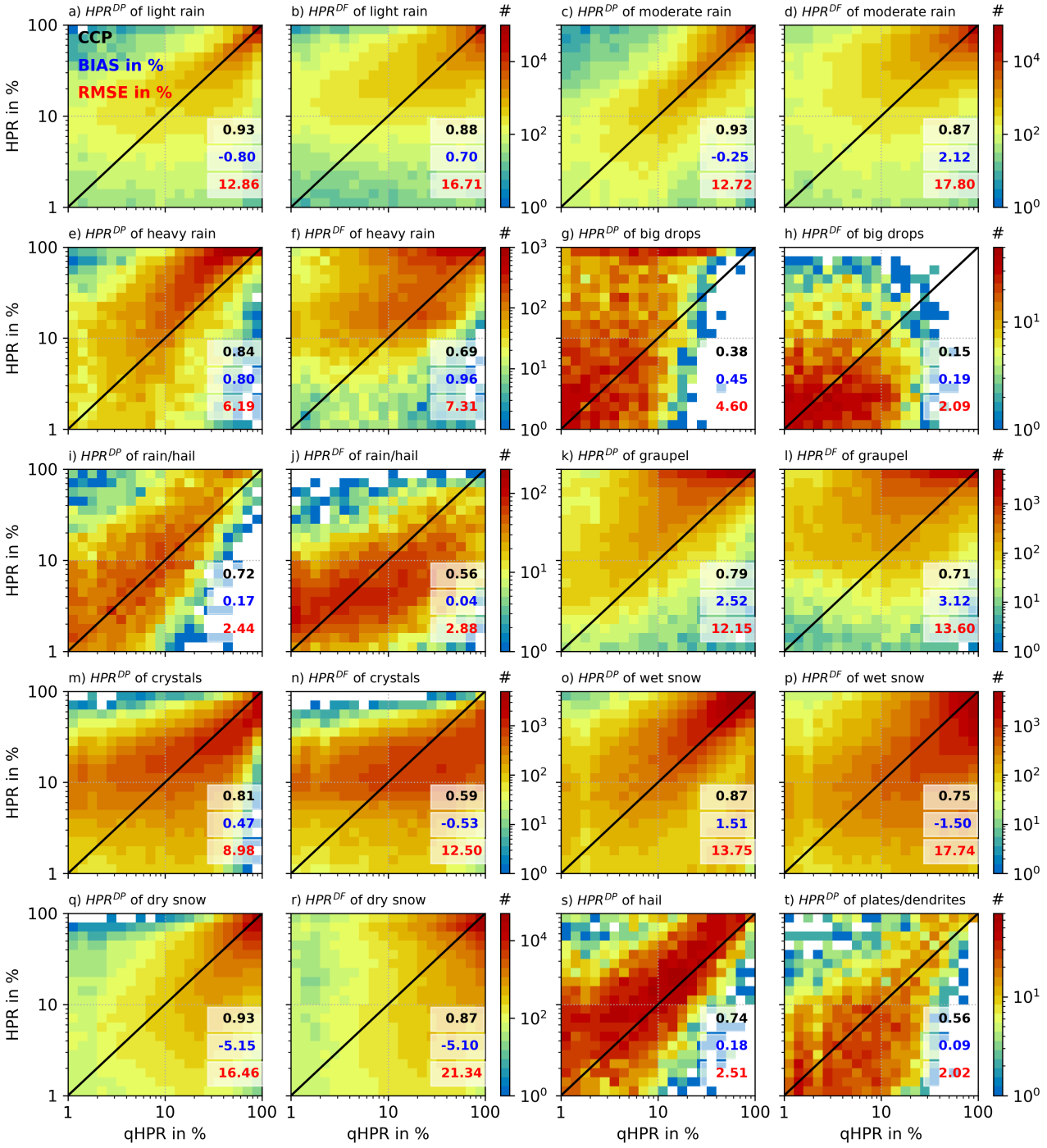

Figure 5. Two-dimensional histograms of the pairwise comparison $\mathrm{HPR}_\mathrm{k}^\mathrm{DF}$ and $\mathrm{HPR}_\mathrm{k}^\mathrm{DP}$ with qHPR for the different hydrometeor classes. The CCP, BIAS and RMSE are in black, blue and red. The colors indicate the count of samples and the black solid line the 1:1 relationship.

Until 50 km range, enhanced Z_{DR} and DFR and moderate Z_{Ku}^{m} and Z_{H} values result in corresponding increased HPR_{k}^{DF} and HPR_{k}^{DP} of moderate rain and low HPR_{k}^{DF} and HPR_{k}^{DP} of light rain (Fig. 7a, b and Fig. 8a, b). HPR_{k}^{DF} of big drops appears with low ratios in the convective region, whereas HPR_{k}^{DP} of big drops does not show a clear signal. In a range between 10 km to 30 km the small-scale convective regions are not detected by the DPR resulting in no big drops HPR_{k}^{DF} where small proportions of HPR_{k}^{DP} are still estimated (Fig. 7d and Fig. 8d). DP estimates effectively illustrate the transition from solid hydrometeors such as dry snow via wet snow to liquid hydrometeors such as light rain, moderate rain and heavy rain. However, wet snow HPR_{k}^{DF} do not match with DPRs bright-band detection where HPR_{k}^{DP} of wet snow is restricted between $T_{b} = 0°C$ and $T_{t} = 4°C$ (Fig. 7h and Fig. 8h). Heavy rain is apparent in DP measurements within the ML, which is not the case in the DF measurements (Fig. 7c and Fig. 8c).

Both DF and DP measurements allocate the transition zone from ice to snow retrievals at approximately 8 km altitude, which corresponds to the height of the DGL (Fig. 7g, i and Fig. 8g, i) identified by increased K_{DP} values slightly above the $-15°C$ isotherm (Fig. 6f). In the measurements obtained at ranges up to 20 km a decrease in K_{DP} and an increase in Z_{H} can be identified below the $-15°C$ isotherm (Fig. 6b, d and f) indicating aggregation processes (Trömel et al., 2019). This is also supported by increasing DFR measurements in the same region (Fig. 6g). Increased snow HPRs above the $-15°C$ isotherm may be connected to the underestimation of ice HPRs, as identified in Sect.4.2. The partial occurrence of HPR_{k}^{DP} of plates/dendrites in the DGL (Fig. 8j) is challenging to interpret due to the differential attenuation (Fig. 6d).

As expected rimed hydrometeors like GP, RH and HA, are primarily observed in convective regime. Due to the discrepancy between RT classifications based on GR and SR measurements (f in Fig. 7 and Fig. 8) high graupel HPR_{k}^{DF} extend over a larger region compared to HPR_{k}^{DP} of graupel. Overall HPR of graupel in DP and DF are significantly overestimated (compare Sect.4.2). A comparison of hail HPRs reveal a comparable vertical distribution up to an altitude of approximately 8 km. Note that rain/hail and hail HPR_{k}^{DP} (Fig. 8e and k) have to be considered combined for a direct comparison with rain/hail HPR_{k}^{DF} (Fig. 6e). In regions with NBF, the detection of hail has to be considered with caution due the similarity of the DP signals for NBF and hail. However, SR partially confirms hail HPR in these areas. Due to the overall overestimation (underestimation) of hail HPRs in DP (DF) space, according estimates should be treated with caution.

5 Conclusions

This paper describes the most recent improvements of a more sophisticated hydrometeor classification (HMC) scheme to derive also hydrometeor partitioning ratios (HPRs). Such an algorithm has been first introduced by Besic et al. (2018) and enhanced in Trömel et al. (2023) (HMC_{P}). HMC_{P} is capable to derive HPRs from dual-polarization (DP) measurements (HMC_{P}^{DP}) of ground-based radars (GR) for each resolved volume. Combining GR DP observations from NEXRAD's WSR-88D S-band radars with space-borne radar (SR) dual-frequency (DF) observations, more precisely from the Dual-Frequency Precipitation Radar (DPR) onboard the Global Precipitation Measurement core satellite (GPM), allows to extend HMC_{P} for DF-based HPR estimates from SR observations (HMC_{P}^{DF}). Matching SR and GR observations, superobbed volumes containing a large number of GR pixels are generated and enable the estimation of quasi HPRs (qHPRs). These qHPRs represent the hydrometeor

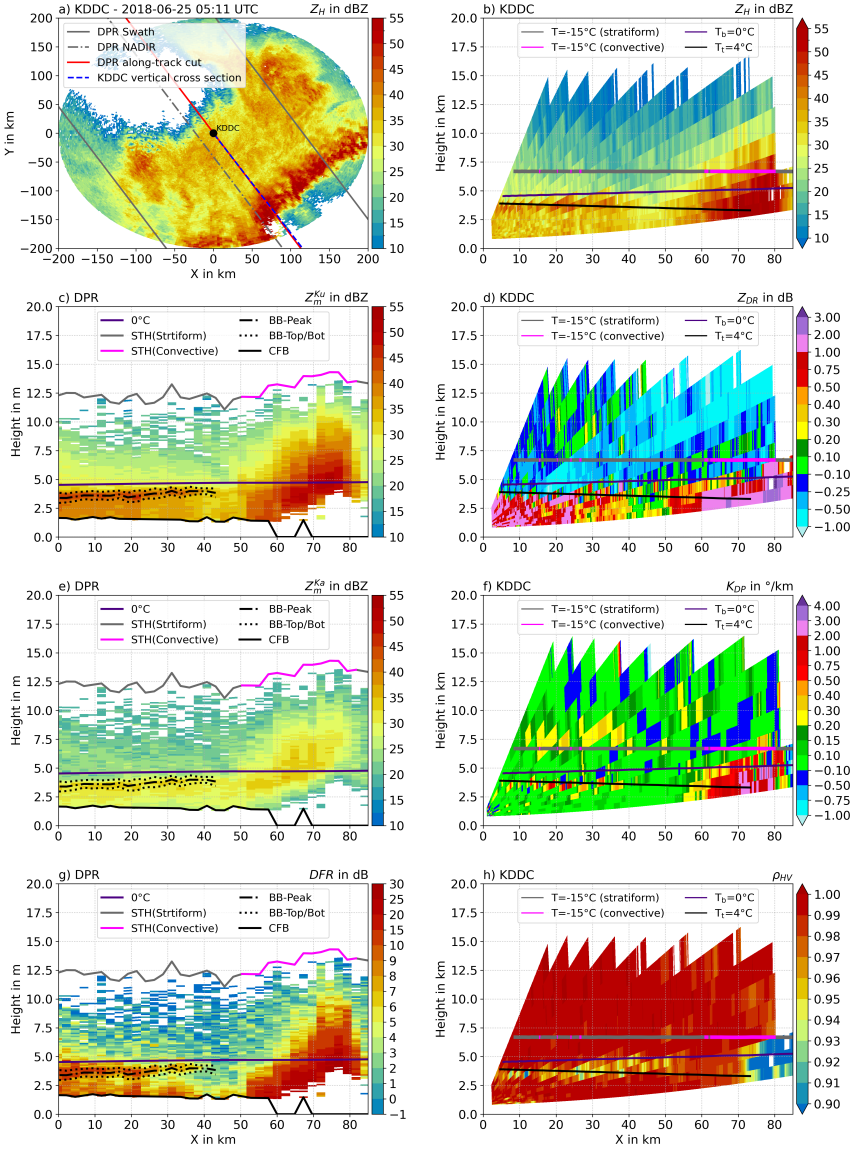

Figure 6. a) PPI of Z_H measured on 25 June 2018 at 05:11 UTC with KDDC and overpassed by GPM (orbit number 024557). Nadir along-track vertical cut of DPR-observed Z_{Ku}^m (c), Z_{Ka}^m (e) and DFR (g). Pseudo RHIs of Z_H (b), Z_{DR} (d), K_{DP} (f), ρ_{HV} (h) along DPR's vertical cut. In panel a the gray lines indicate DPRs outer swath, the gray dashed line DPRs NADIR scan, the red line the along-track vertical cut and the blue line the location of the vertical cross section of the GR. In panels c, e and g the black line indicates the clutter free bottom, the indigo line the freezing level height (DPR), and the STH for convective (magenta) and for stratiform (cyan) SR-based RT. The dashed lines represent the bright band top and bottom. The bright band peak is illustrated as dash-dotted line. In panels b, d, f and h the black lines indicate the $T_t = 4°C$ and the indigo lines the $T_b = 0°C$ isotherms. The $T = -15°C$ is indicated in gray/magenta for the GR-based stratiform/convective RT.

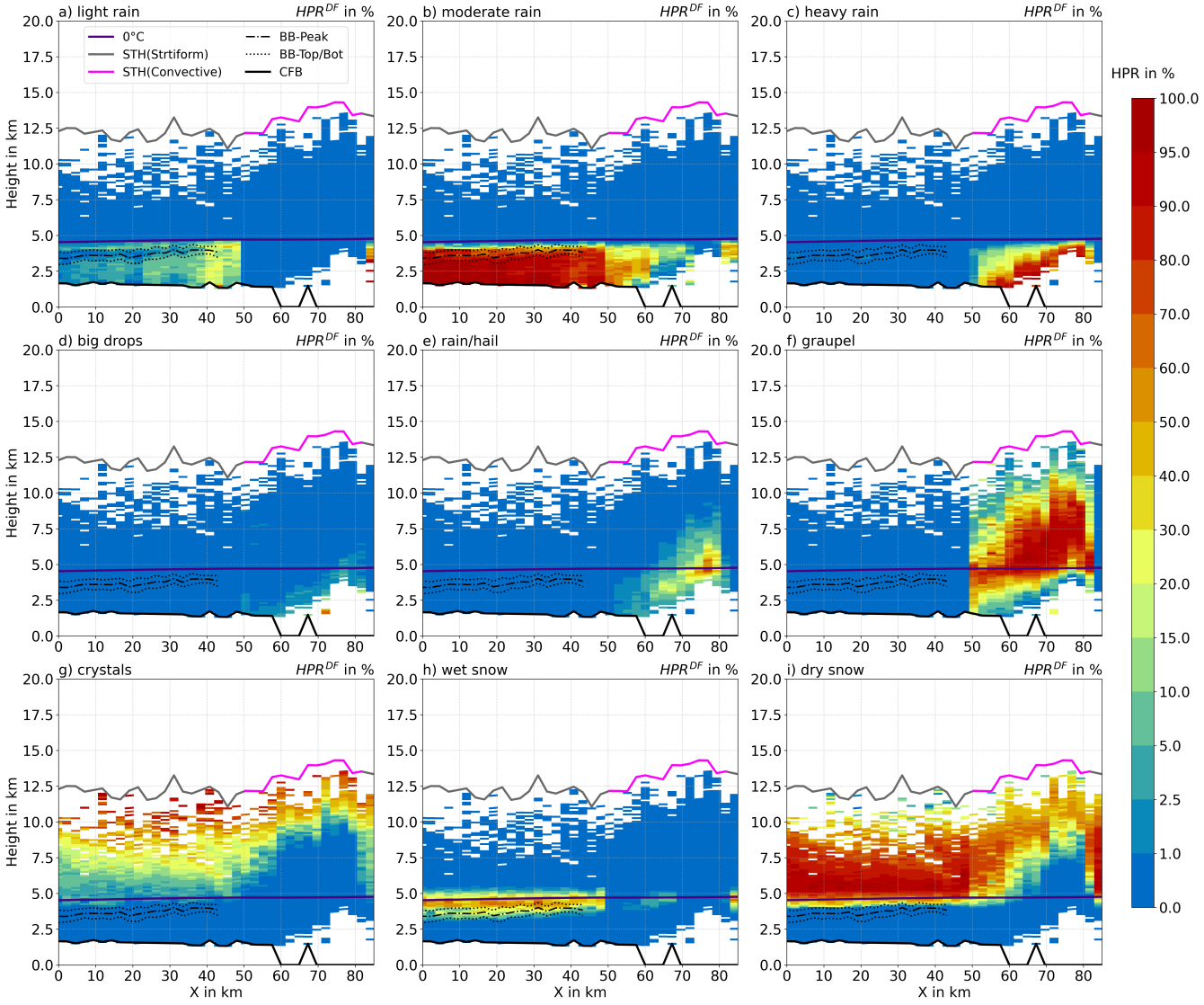

Figure 7. Estimated $\mathrm{HPR_k^{DF}}$ for different hydrometeor classes applying $\mathrm{HMC_P}$ to SR observations shown in Fig. 6. The black line indicates the clutter free bottom, the indigo line the freezing level height (DPR), and the STH for convective (magenta) and for stratiform (gray) SR-based RT. The dashed lines represent the bright band top and bottom. The bright band peak is illustrated as dash-dotted line.

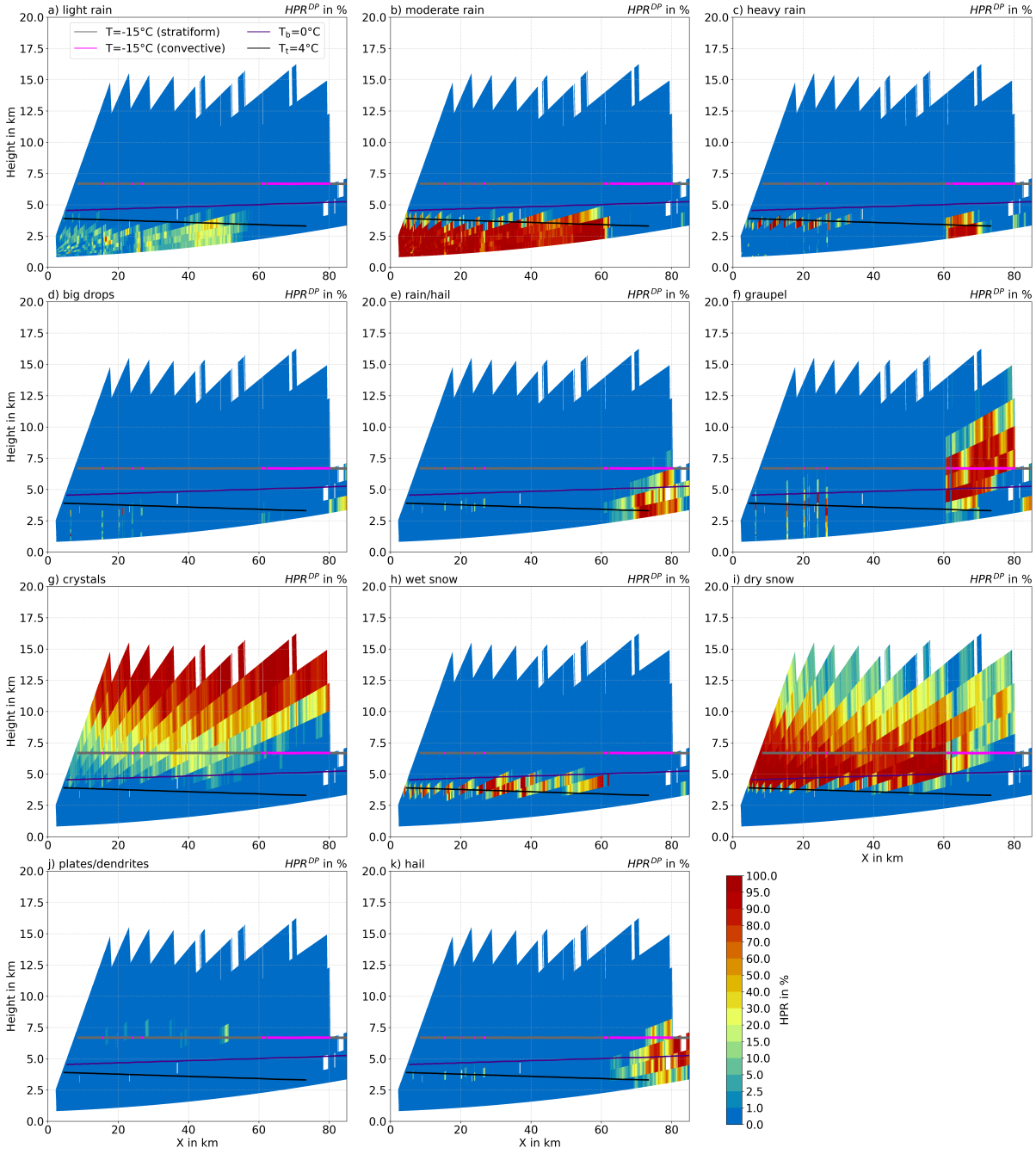

Figure 8. Estimated $\mathrm{HPR}_{\mathrm{k}}^{\mathrm{DP}}$ for different hydrometeor classes with $\mathrm{HMC}_{\mathrm{P}}$ with GR observations shown in Fig. 6 The black lines indicate the $\mathrm{T}_{\mathrm{t}} = 4°C$ and the indigo lines the $\mathrm{T}_{\mathrm{b}} = 0°C$ isotherms. The $\mathrm{T}_{\mathrm{c}} = -15°C$ is indicated in gray/magenta for the GR-based stratiform/-convective RT.

mixtures in superobbed volumes and are calculated with the identified dominant hydrometeor classes applying the modified standard HMC to the high-resolution GR measurements. The averaged DF and DP variables and qHPRs of the supperobbed volumes are exploited for the training of $\mathrm{HMC_P}$ and also for the ensuing evaluation of HPR estimates. Such estimates are either based on DP ($\mathrm{HPR_k^{DP}}$) or DF ($\mathrm{HPR_k^{DF}}$) observations and compared with the qHPRs derived from averaged DF and DP variables, respectively. The derived $\tilde{p}_k$, which form the basis for the $\mathrm{HMC_P}$, are in line with expected DP and DF observations for different hydrometeor classes (e.g. Straka et al., 2000; Bechini and Chandrasekar, 2015; Trömel et al., 2019; Thompson et al., 2014). A comparison between qHPRs and HPRs in DF ($\mathrm{HPR_k^{DF}}$) and DP-space ($\mathrm{HPR_k^{DP}}$) results in correlations higher than 0.7 for various hydrometeor classes. Lowest correlations are obtained for big drops in both DP- and DF-space with 0.38 and 0.15, respectively, followed by correlations for $\mathrm{HPR_k^{DF}}$of ice with 0.59, dendrites/plates and rain/hail both with 0.56. $\mathrm{HMC_P}$ overestimates graupel and underestimates snow HPRs in DF and DP space. Hail HPRs are overestimated in DP and slightly underestimated in DF space. Overall, HPR estimates are more accurate in DP space than in DF space and perform best for liquid hydrometeors, except for big drops. DP observation provide additional information e.g. on the shape, orientation and homogeneity of the hydrometeors within the measurement volume compared to DF observations leads to more accurate derivations of HPR. Furthermore, $\mathrm{HMC_P^{DP}}$ and $\mathrm{HMC_P^{DF}}$ have been trained with DP data, also promoting a better performance in DP space. A case study revealed a high degree of agreement between GR- and SR-based estimates as well as a plausible vertical distribution of HPRs in the light of the DF and DP measurements.

Including additional information in the multidimensional observation vectors $\boldsymbol{X}_\mathrm{i}^\mathrm{DF}$ and $\boldsymbol{X}_\mathrm{i}^\mathrm{DP}$ could further improve the accuracy of the HPR estimates. E.g., for $\boldsymbol{X}_\mathrm{i}^\mathrm{DF}$ vertical gradients of $\mathrm{Z_{Ku}^m}$ or DFR can be exploited. Battaglia et al. (2014), Mroz et al. (2018) and Le et al. (2016) demonstrated already their information content for the detection of hail and wet snow. Observations from other satellite devices, e.g. brightness temperatures from GPMs passive microwave radiometer utilized for hail (Mroz et al., 2017) or snow (Rysman et al., 2018, 2019) detection, could also be exploited to increase the information content. With respect to GR observations, the depolarization ratio, which has been shown to be valuable for riming detection (Blanke et al., 2024), might extend $\boldsymbol{X}_\mathrm{i}^\mathrm{DP}$.

The retrievals introduced in this paper can be considered as valuable for different meteorological aspects. E.g., more accurate hydrometeor classifications can refine the calibration of GR with SR observations (Cao et al., 2013; Pejcic et al., 2022) by adapting the frequency transformation much more precisely to specific hydrometeor classes. Using $\mathrm{HMC_P^{DF}}$, the GPM DPRs area-wide measurements now provide precise information on hydrometeor distributions in areas without GR measurements. This allows e.g. to extend the evaluation of hydrometeor distributions in numerical weather prediction (NWP) models (Trömel et al., 2023) to the global scale. The assimilation of GR-based measurements and retrievals (Trömel et al., 2023; Reimann et al., 2023), but also of SR-based reflectivity measurements (Ikuta et al., 2021; Kotsuki et al., 2023) and rainfall estimates Li et al. (2020) in NWP has been shown to improve the accuracy of numerical precipitation prediction. Thus, the assimilation of DF- and DP-based HPRs may further improve the representation of hydrometeors in NWP.

Code and data availability. Codes for the data processing and intermediate data products can be made available upon request. HMC_P is available at ωradlib.The GPM data can be downloaded following Iguchi and Meneghini (2021) and the quality-controlled ground radar data can be requested by NASA's GPM Ground Validation program (GPM-GV).

Appendix A: Processing of ground-based radar observations

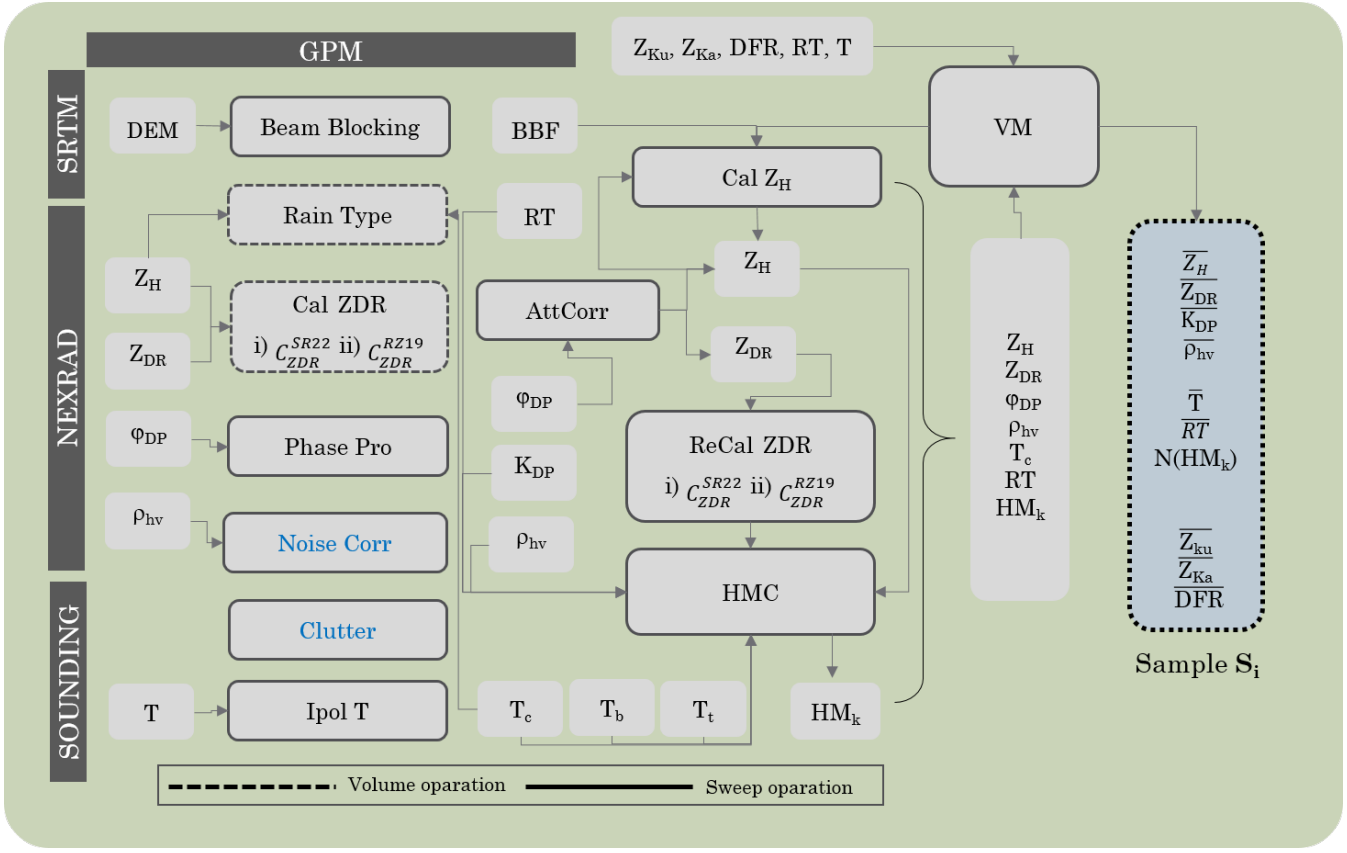

Figure A1. Workflow for polarimetric radar data processing of the NEXRAD S-band weather radars (gray boxes). The black boxes represent the different data sources used and the gray boxes outlined with solid or dashed lines represent processing operations based on a sweep or volume data, respectively. Operations that have already been performed on the NEXRAD data are written in blue.

In the following the GR processing is explained in more detail (Fig. A1). Digital Elevation Model (DEM) data from the Shuttle Radar Topography Mission (SRTM, Reuter et al. (2007)) is used to calculate any possible beam blocking fractions (BBF) following Bech et al. (2003). Z_H is smoothed with a moving average of 5 range bins, while 11 range bins are used to smooth Z_{DR} and ρ_{HV}. A ρ_{HV} threshold of 0.8 is applied for the noise filtering. In the next step, the rain type classification following Park et al. (2009) is applied to the entire volume to classify convective and stratiform radar bins, but with slight modifications (i.e., the classification as convective based on ρ_{HV} only is omitted).

For Z_{DR} calibration, either the method using Quasi-Vertical-Profiles (Sanchez-Rivas and Rico-Ramirez, 2022) in the following referred to $Cal_{Z_{DR}}^{SR22}$ or the Z_H-Z_{DR} consistency in light rain (Ryzhkov and Zrnic, 2019), referred as $Cal_{Z_{DR}}^{RZ19}$, is applied. Since the data base is limited to volume scans for specific time steps only, $Cal_{Z_{DR}}^{SR22}$ is not applied to Quasi-Vertical-Profiles but to all available PPI scans to include a larger amount of data in the calibration routine. Slight modifications of $Cal_{Z_{DR}}^{SR22}$ include the application of the median instead of the mean (Eq. 10; Sanchez-Rivas and Rico-Ramirez, 2022) for noise filtering and recalculation of the intrinsic mean Z_{DR} (0.178 dB) for the S-band data. A first guess Z_{DR}-offset, using either $Cal_{Z_{DR}}^{SR22}$ or $Cal_{Z_{DR}}^{RZ19}$ if there are less then 1000 valid radar bins, is applied on the entire volume scan before the final recalculated Z_{DR}-offset is applied after correction for (differential) attenuation sweep-wise. Valid observations for the Z_{DR}-offset calibration are all radar bins with ρ_{HV}> 0.99, T_t>5°C and if applying $Cal_{Z_{DR}}^{SR22}$ 0 dBZ$\leq Z_H \leq$20 dBZ otherwise 20 dBZ$\leq Z_H \leq$30 dBZ for $Cal_{Z_{DR}}^{RZ19}$.

The processing of differential Phase ϕ_{DP} includes radial smoothing with a window size of 9 radar bins for measurements Z_H >40 dBZ (heavy rain) and a window size of 25 radar bins elsewhere (Park et al., 2009). Instead of determining K_{DP} based on the slope of a least squares fit, a low-noise Lanczos differentiator (Heistermann et al., 2013; Diekema and Koornwinder, 2012) is used to speed up the processing significantly. The two window sizes are also applied for the K_{DP} derivation. Correction for (differential) attenuation applies parameters $\alpha = 0.04\,\mathrm{dB\,deg^{-1}}$ and $\beta = 0.004\,\mathrm{dB\,deg^{-1}}$ (Ryzhkov and Zrnic, 1995). The attenuation correction is limited to the liquid phase ($T_t > 4°C$) and the highest values of the path-integrated attenuation (PIA) and path-integrated differential attenuation (PIDA) reached in the liquid phase are applied to the remaining mixed phase and solid radar observations.

Z_H calibration (Cal_{ZH}) is performed by comparing the GR with SR measurements (Pejcic et al., 2022; Crisologo and Heistermann, 2020; Warren et al., 2018; Louf and Protat, 2023; Protat et al., 2022). GR and SR measurements are matched to the same geometry for each volume scan (more detailed description in Sect. 2.3), but measurements contaminated by the ML are excluded from the offset calculations (Pejcic et al., 2022). For this purpose, the ML top and bottom estimates determined by the DPR are used. The conversion of reflectivity from Ku-band to S-band wavelengths is performed following Cao et al. (2013). Further refinements of Cal_{ZH} include the use of quality indices, determined from BBF and PIA, as weighting factors for determining the Z_H-offset (Crisologo and Heistermann, 2020).

Appendix B: The standard Hydrometeor Classification to identify the dominant hydrometeor class

The membership functions (MSFs, Tab. B1) for the hydrometeor classes heavy rain, big drops , rain/hail, wet snow and graupel are adapted from Park et al. (2009), whereas the rain class is subdivided into the light rain and moderate rain classes with a Z_H threshold of 28 dBZ (Tab. B1 light rain and moderate rain columns) following Straka et al. (2000). The big drops hydrometeor class originates from (Park et al., 2009) and represents rain with a skewed drop size distribution towards larger raindrops, indicating the presence of raindrops with a diameter greater than 3 mm and a lack of smaller raindrops. Furthermore, the Z_{DR} MSF for crystals is extended to negative values and the Z_H MSF for dry snow and crystals includes the snow ice switch-over between 15 dBZ and 20 dBZ (Tab. B1 dry snow and crystals column) following Thompson et al. (2014).

Plates/dendrites is added as a new class combining the MSFs of plates and dendrites from Thompson et al. (2014). For this purpose, the MSFs of the two hydrometeor classes are superimposed and only the outer boundaries are considered (Tab. B1 plates/dendrites column). The ρ_{HV}-MSF for crystals are used also for plates/dendrites. For hail, the polarimetric MSF from Dolan et al. (2013) are applied. In general the trapezoidal MSFs of hail and plates/dendrites are tuned until they overlap as good as possible with the membership beta functions used in Dolan et al. (2013) and Thompson et al. (2014).

The temperature MSFs are designed to allow solid phase hydrometeors crystals and dry snow only at temperatures below 0°C and liquid phase hydrometeors at temperatures above 0°C. Wet snow and plates/dendrites are restricted to temperature regimes with their highest probability of occurrence (von Terzi et al., 2022; Lundquist et al., 2008; Heymsfield et al., 2021) and hydrometeors such as rain/hail, big drops, hail and graupel are allowed to exist in all regions (liquid, solid and mixed phase). Big drops are restricted up to -32.5°C assuming the $6.5^{\circ}\mathrm{C}/\mathrm{km}$ lapse rate. This corresponds to findings of van Lier-Walqui et al. (2016) reporting updrafts reaching around 5 km above the freezing level. Graupel MSF for temperature are set to the temperature interval between -50 $^{\circ}C$ and 30 $^{\circ}C$, which is consistent with the boundaries for high density and low density graupel in Dolan et al. (2013).

Appendix C: List of abbreviations

Table B1. Values x1, x2, x3 and x4 of the used trapezoidal membership functions for Z_H, Z_{DR}, LK_{DP}, ρ_{HV} and T. f1, f2, f3, g1 and g2 can be found in Park et al. (2009) Eq.4 and Eq.5

	light rain	moderate rain	heavy rain	big drops	rain hail	graupel	crystals	dry snow	wet snow	plates dendrites	hail
x1(Z_H) in dBZ	**5.0**	**23.0**	40.0	20.0	45.0	25.0	0.0	**15.0**	25.0	**-1.0**	**45.0**
x2(Z_H) in dBZ	**10.0**	**28.0**	45.0	25.0	50.0	35.0	5.0	**20.0**	30.0	**2.0**	**50.0**
x3(Z_H) in dBZ	**28.0**	**45.0**	55.0	45.0	75.0	50.0	**15.0**	35.0	40.0	**26.0**	**67.0**
x4(Z_H) in dBZ	**33.0**	**50.0**	60.0	50.0	80.0	55.0	**20.0**	40.0	50.0	**31.0**	**72.5**
x1(Z_{DR}) in dB	f1-0.3	f1-0.3	f1-0.3	f2-0.3	-0.3	-0.3	**-1.0**	-0.3	0.5	**1.3**	**-0.5**
x2(Z_{DR}) in dB	f1	f1	f1	f2	0.0	0	**-0.8**	0.0	1.0	**1.6**	**-0.25**
x3(Z_{DR}) in dB	f2	f2	f2	f3	f1	f1	3.0	0.3	2.0	**8.4**	**0.50**
x4(Z_{DR}) in dB	f2+0.5	f2+0.5	f2+0.5	f3+1	f1+0.5	f1+0.5	3.3	0.6	3.0	**9.2**	**0.75**
x1(LK_{DP})	g1-1	g1-1	g1-1	g1-1	-10.0	-30.0	-5.0	-30.0	-30.0	**-30.0**	**-30.0**
x2(LK_{DP})	g1	g1	g1	g1	-4.0	-25.0	0.0	-25.0	-25.0	**-13.0**	**-29.0**
x3(LK_{DP})	g2	g2	g2	g2	g1	10.0	10.0	10.0	10.0	**-3.0**	**4.8**
x4(LK_{DP})	g2+1	g2+1	g2+1	g2+1	g1+1	20.0	15.0	20.0	20.0	**2.15**	**7.0**
x1(ρ_{HV})	0.95	0.95	0.92	0.92	0.85	0.90	0.95	0.95	0.88	**0.94**	**0.80**
x2(ρ_{HV})	0.97	0.97	0.95	0.95	0.90	0.97	0.98	0.98	0.92	**0.97**	**0.91**
x3(ρ_{HV})	1.00	1.00	1.00	1.00	1.00	1.00	1.00	1.00	0.95	**0.99**	**0.99**
x4(ρ_{HV})	1.01	1.01	1.01	1.01	1.01	1.01	1.01	1.01	0.985	**1.00**	**1.00**
x1(T) in $°C$	**0.0**	**0.0**	**0.0**	**-32.5**	**-90.0**	**-50.0**	**-90.0**	**-90.0**	**-2.0**	**-20.0**	**-90.0**
x2(T) in $°C$	**1.0**	**1.0**	**1.0**	**-19.5**	**-50.0**	**-40.0**	**-80.0**	**-80.0**	**0.0**	**-17.5**	**-50.0**
x3(T) in $°C$	**50.0**	**50.0**	**50.0**	**50.0**	**50.0**	**5.0**	**-2.0**	**-2.0**	**4.0**	**-12.5**	**0.0**
x4(T) in $°C$	**55.0**	**55.0**	**55**	**55.0**	**55.0**	**30.0**	**0.0**	**0.0**	**6.0**	**-10.0**	**5.0**

Author contributions. VP developed the methodology for this work, designed the manuscript, performed the coding, processed the data and carried out the visualization and analysis. KMu supported the code for the VMM. ST and KMr provided the scientific advice and support in the development of the text.

Competing interests. The authors state that they have no conflict of interest.

Acknowledgements. Velibor Pejcic's research was carried out partially in the framework of the priority programme SPP 2115 "Polarimetric Radar Observations meet Atmospheric Modelling (PROM)" within the project "Operation Hydrometeors" and the research project Near-Realtime Precipitation Estimation and Prediction (RealPEP). Work done by Kamil Mroz was performed under a contract with the National Centre for Earth Observation. We would also like to extend our gratitude to Jason Pippitt and Daniel Watters for providing and supporting

Table C1. Frequently used non-mathematical abbreviations separated in overall abbreviations (top) and abbreviations used for space-bor (center) and ground based observations (bottom)

HMC – hydrometeor classifications	ML – melting layer
VMM - volume matching method	$\mathrm{HMC_P}$– HMC following Trömel et al. (2023)
$\mathrm{HMC_Z}$– HMC following Zrnić et al. (2001b)	HPR – hydrometeor partitioning ratio
qHPR – quasi hydrometeor partitioning ratio	DGL – dendritic growth layer
ML – melting layer	RT – rain type
DEM - Digital Elevation Model	SRTM - Shuttle Radar Topography Mission
SR – space-borne radar	DF – dual-frequency
$\mathrm{HMC_P^{DF}}$– extended $\mathrm{HMC_P}$for DF	$\mathrm{HPR_k^{DF}}$– DF derived HPRs
GPM - Global Precipitation Measuring core satellite	DPR - Dual-Frequency Precipitation Radar
TRMM - Tropical Rainfall Measuring Mission	PR - Precipitation Radar
GMI - GPMs Microwave Imager	STH – storm top height
KaPR – Ka-band precipitation radar	KuPR – Ku-band precipitation radar
$\mathrm{Z_{Ku}^m}$– measured Ku-band reflectivity	$\mathrm{Z_{Ka}^m}$– measured Ka-band reflectivity
DFR– dual-frequency ratio	PTI - precipitation type index
GR – ground-based radar	DP – dual-polarization
$\mathrm{HMC_P^{DP}}$– refined $\mathrm{HMC_P}$based on DP	$\mathrm{HPR_k^{DP}}$– DP derived HPRs
PIA - path-integrated attenuation	PIDA - path-integrated differential attenuation
$\mathrm{Z_H}$ – horizontal reflectivity	$\mathrm{Z_{DR}}$ – differential reflectivity
$\mathrm{K_{DP}}$ – specific differential phase	ρ_{HV} – cross correlation coefficient
BBF - beam blocking fractions	$\mathrm{LK_{DP}}$ – log-transformed $\mathrm{K_{DP}}$
$\mathrm{T_c}$ – temperature at the beam center	$\mathrm{T_t}$ – temperature at top beam edge
$\mathrm{T_b}$ – temperature at bottom beam edge	$\mathrm{Cal_{ZH}}$ - $\mathrm{Z_H}$-calibration with SR
$\mathrm{Cal_{Z_{DR}}^{SR22}}$ - $\mathrm{Z_{DR}}$-calibration (Sanchez-Rivas and Rico-Ramirez, 2022)	$\mathrm{Cal_{Z_{DR}}^{RZ19}}$ - $\mathrm{Z_{DR}}$-calibration (Ryzhkov and Zrnic, 2019)

us with the GPM GV GR data and also thank NASA/JAXA for providing the GPM DPR data. Furthermore, we would like to express our gratitude to Julian Steinheuer for his scientific support.

Financial support. This research was funded by the German Research Foundation (Deutsche Forschungsgemeinschaft, DFG; 320397309 and 408027387).

References

Ackermann, L., Soderholm, J., Protat, A., Whitley, R., Ye, L., and Ridder, N.: Radar and environment-based hail damage estimates using machine learning, Atmospheric Measurement Techniques Discussions, 2023, 1–24, https://doi.org/https://doi.org/10.5194/amt-17-407-2024, 2023.

Battaglia, A., Tanelli, S., Heymsfield, G. M., and Tian, L.: The dual wavelength ratio knee: A signature of multiple scattering in airborne Ku–Ka observations, Journal of Applied Meteorology and Climatology, 53, 1790–1808, https://doi.org/https://doi.org/10.1175/JAMC-D-13-0341.1, 2014.

Bech, J., Codina, B., Lorente, J., and Bebbington, D.: The sensitivity of single polarization weather radar beam blockage correction to variability in the vertical refractivity gradient, Journal of Atmospheric and Oceanic Technology, 20, 845–855, https://doi.org/https://doi.org/10.1175/1520-0426(2003)020<0845:TSOSPW>2.0.CO;2, 2003.

Bechini, R. and Chandrasekar, V.: A Semisupervised Robust Hydrometeor Classification Method for Dual-Polarization Radar Applications, Journal of Atmospheric and Oceanic Technology, 32, 22 – 47, https://doi.org/https://doi.org/10.1175/JTECH-D-14-00097.1, 2015.

Besic, N., Figueras i Ventura, J., Grazioli, J., Gabella, M., Germann, U., and Berne, A.: Hydrometeor classification through statistical clustering of polarimetric radar measurements: A semi-supervised approach, Atmospheric Measurement Techniques, 9, 4425–4445, https://doi.org/10.5194/amt-9-4425-2016, 2016.

Besic, N., Gehring, J., Praz, C., Figueras i Ventura, J., Grazioli, J., Gabella, M., Germann, U., and Berne, A.: Unraveling hydrometeor mixtures in polarimetric radar measurements, Atmospheric Measurement Techniques, 11, 4847–4866, https://doi.org/10.5194/amt-11-4847-2018, 2018.

Billault-Roux, A.-C., Ghiggi, G., Jaffeux, L., Martini, A., Viltard, N., and Berne, A.: Dual-frequency spectral radar retrieval of snowfall microphysics: a physics-driven deep-learning approach, Atmospheric Measurement Techniques, 16, 911–940, https://doi.org/10.5194/amt-16-911-2023, 2023.

Blanke, A., Gergely, M., and Trömel, S.: A new aggregation and riming discrimination algorithm based on polarimetric weather radars, EGUsphere, 2024, 1–28, https://doi.org/10.5194/egusphere-2024-3336, 2024.

Cao, Q., Hong, Y., Qi, Y., Wen, Y., Zhang, J., Gourley, J. J., and Liao, L.: Empirical conversion of the vertical profile of reflectivity from Ku-band to S-band frequency, Journal of Geophysical Research: Atmospheres, 118, 1814–1825, https://doi.org/https://agupubs.onlinelibrary.wiley.com/doi/full/10.1002/jgrd.50138, 2013.

Chen, H., Chandrasekar, V., and Bechini, R.: An Improved Dual-Polarization Radar Rainfall Algorithm (DROPS2.0): Application in NASA IFloodS Field Campaign, Journal of Hydrometeorology, 18, 917 – 937, https://doi.org/https://doi.org/10.1175/JHM-D-16-0124.1, 2017.

Cifelli, R., Chandrasekar, V., Lim, S., Kennedy, P. C., Wang, Y., and Rutledge, S. A.: A New Dual-Polarization Radar Rainfall Algorithm: Application in Colorado Precipitation Events, Journal of Atmospheric and Oceanic Technology, 28, 352 – 364, https://doi.org/https://doi.org/10.1175/2010JTECHA1488.1, 2011.

Crisologo, I. and Heistermann, M.: Using ground radar overlaps to verify the retrieval of calibration bias estimates from spaceborne platforms, Atmospheric Measurement Techniques, 13, 645–659, https://doi.org/https://doi.org/10.5194/amt-13-645-2020, 2020.

Diekema, E. and Koornwinder, T. H.: Differentiation by integration using orthogonal polynomials, a survey, Journal of Approximation Theory, 164, 637–667, https://doi.org/https://doi.org/10.1016/j.jat.2012.01.003, 2012.

Dolan, B. and Rutledge, S. A.: A theory-based hydrometeor identification algorithm for X-band polarimetric radars, Journal of Atmospheric and Oceanic Technology, 26, 2071–2088, https://doi.org/10.1175/2009JTECHA1208.1, 2009.

Dolan, B., Rutledge, S. A., Lim, S., Chandrasekar, V., and Thurai, M.: A robust C-band hydrometeor identification algorithm and application to a long-term polarimetric radar dataset, Journal of Applied Meteorology and Climatology, 52, 2162–2186, https://doi.org/10.1175/JAMC-D-12-0275.1, 2013.

Gehring, J., Oertel, A., Vignon, E., Jullien, N., Besic, N., and Berne, A.: Microphysics and dynamics of snowfall associated with a warm conveyor belt over Korea, Atmospheric Chemistry and Physics, 20, 7373–7392, https://doi.org/10.5194/acp-20-7373-2020, 2020.

Gehring, J., Vignon, É., Billault-Roux, A.-C., Ferrone, A., Protat, A., Alexander, S. P., and Berne, A.: Orographic flow influence on precipitation during an atmospheric river event at Davis, Antarctica, Journal of Geophysical Research: Atmospheres, 127, e2021JD035 210, https://doi.org//10.1029/2021JD035210, 2022.

Giangrande, S. E. and Ryzhkov, A. V.: Estimation of rainfall based on the results of polarimetric echo classification, Journal of applied meteorology and climatology, 47, 2445–2462, https://doi.org/https://doi.org/10.1175/2008JAMC1753.1, 2008.

Grazioli, J., Tuia, D., and Berne, A.: Hydrometeor classification from polarimetric radar measurements: a clustering approach, Atmospheric Measurement Techniques, 8, 149–170, https://doi.org/10.5194/amt-8-149-2015, 2015.

Heistermann, M., Jacobi, S., and Pfaff, T.: Technical Note: An open source library for processing weather radar data (wradlib), Hydrology and Earth System Sciences, 17, 863–871, https://doi.org/10.5194/hess-17-863-2013, 2013.

Heymsfield, A. J., Bansemer, A., Theis, A., and Schmitt, C.: Survival of snow in the melting layer: Relative humidity influence, Journal of the Atmospheric Sciences, 78, 1823–1845, https://doi.org/https://doi.org/10.1175/JAS-D-20-0353.1, 2021.

Hou, A. Y., Kakar, R. K., Neeck, S., Azarbarzin, A. A., Kummerow, C. D., Kojima, M., Oki, R., Nakamura, K., and Iguchi, T.: The global precipitation measurement mission, Bulletin of the American meteorological Society, 95, 701–722, https://doi.org//10.1175/BAMS-D-13-00164.1, 2014.

Iguchi, T. and Meneghini, R.: GPM DPR Precipitation Profile L2A 1.5 hours 5 km V07, Greenbelt, MD, Goddard Earth Sciences Data and Information Services Center (GES DISC), Accessed: 2024, Goddard Earth Sciences Data and Information Services Center (GES DISC), https://doi.org/https://doi.org/10.5067/GPM/DPR/GPM/2A/07, 2021.

Iguchi, T., Seto, S., Meneghini, R., Yoshida, N., Awaka, J., Le, M., Chandrasekar, V., and Kubota, T.: GPM/DPR level-2 algorithm theoretical basis document, NASA Goddard Space Flight Center, 2010.

Iguchi, T., Kawamoto, N., and Oki, R.: Detection of intense ice precipitation with GPM/DPR, Journal of Atmospheric and Oceanic Technology, 35, 491–502, https://doi.org/https://doi.org/10.1175/JTECH-D-17-0120.1, 2018.

Ikuta, Y., Okamoto, K., and Kubota, T.: One-dimensional maximum-likelihood estimation for spaceborne precipitation radar data assimilation, Quarterly Journal of the Royal Meteorological Society, 147, 858–875, https://doi.org/https://doi.org/10.1002/qj.3950, 2021.

Jang, S., Lim, K.-S. S., Ko, J., Kim, K., Lee, G., Cho, S.-J., Ahn, K.-D., and Lee, Y.-H.: Revision of WDM7 microphysics scheme and evaluation for precipitating convection over the Korean peninsula, Remote Sensing, 13, 3860, https://doi.org//10.3390/rs13193860, 2021.

Kotsuki, S., Terasaki, K., Satoh, M., and Miyoshi, T.: Ensemble-Based Data Assimilation of GPM DPR Reflectivity: Cloud Microphysics Parameter Estimation With the Nonhydrostatic Icosahedral Atmospheric Model (NICAM), Journal of Geophysical Research: Atmospheres, 128, e2022JD037 447, https://doi.org/https://doi.org/10.1029/2022JD037447, 2023.

Kubota, T., Masaki, T., Kikuchi, G., Ito, M., Higashiuwatoko, T., Kanemaru, K., Takahashi, N., Yamamoto, K., Furukawa, K., and Nio, T.: Evaluation of Effects on Dual-Frequency Precipitation Radar Observations Due to the Orbit Boost of the GPM Core Observatory, in: IGARSS 2024-2024 IEEE International Geoscience and Remote Sensing Symposium, pp. 709–712, IEEE, https://doi.org/https://doi.org/10.1109/IGARSS53475.2024.10641066, 2024.

Le, M. and Chandrasekar, V.: Hydrometeor profile characterization method for dual-frequency precipitation radar onboard the GPM, IEEE Transactions on Geoscience and Remote Sensing, 51, 3648–3658, https://doi.org//10.1109/TGRS.2012.2224352, 2012.

Le, M. and Chandrasekar, V.: Graupel and hail identification algorithm for the dual-frequency precipitation radar (DPR) on the GPM core satellite, Journal of the Meteorological Society of Japan. Ser. II, 99, 49–65, https://doi.org/https://doi.org/10.2151/jmsj.2021-003, 2021a.

Le, M. and Chandrasekar, V.: A new hail product for GPM DPR, in: 2021 IEEE International Geoscience and Remote Sensing Symposium IGARSS, pp. 828–831, IEEE, https://doi.org/https://doi.org/10.1109/IGARSS47720.2021.9553825, 2021b.

Le, M., Chandrasekar, V., and Biswas, S.: Evaluation and validation of GPM dual-frequency classification module after launch, Journal of Atmospheric and Oceanic Technology, 33, 2699–2716, https://doi.org//10.1175/JTECH-D-15-0253.1, 2016.

Le, M., Chandrasekar, V., and Biswas, S.: An algorithm to identify surface snowfall from GPM DPR observations, IEEE Transactions on Geoscience and Remote Sensing, 55, 4059–4071, https://doi.org/https://doi.org/10.1109/TGRS.2017.2687420, 2017.

Li, X., Mecikalski, J. R., Srikishen, J., Zavodsky, B., and Petersen, W. A.: Assimilation of GPM rain rate products with GSI data assimilation system for heavy and light precipitation events, Journal of Advances in Modeling Earth Systems, 12, e2019MS001 618, https://doi.org/https://doi.org/10.1029/2019MS001618, 2020.

Liao, L. and Meneghini, R.: GPM DPR retrievals: Algorithm, evaluation, and validation, Remote Sensing, 14, 843, https://doi.org/https://doi.org/10.3390/rs14040843, 2022.

Liu, Z., Ostrenga, D., Teng, W., and Kempler, S.: Tropical Rainfall Measuring Mission (TRMM) precipitation data and services for research and applications, Bulletin of the American Meteorological Society, 93, 1317–1325, https://doi.org/https://doi.org/10.1175/BAMS-D-11-00152.1, 2012.

Louf, V. and Protat, A.: Real-time monitoring of weather radar network calibration and antenna pointing, Journal of Atmospheric and Oceanic Technology, 40, 823–844, https://doi.org/https://doi.org/10.1175/JTECH-D-22-0118.1, 2023.

Lukach, M., Dufton, D., Crosier, J., Hampton, J. M., Bennett, L., and Neely III, R. R.: Hydrometeor classification of quasi-vertical profiles of polarimetric radar measurements using a top-down iterative hierarchical clustering method, Atmospheric Measurement Techniques Discussions, 2020, 1–33, https://doi.org/10.5194/amt-2020-143, 2020.

Lundquist, J. D., Neiman, P. J., Martner, B., White, A. B., Gottas, D. J., and Ralph, F. M.: Rain versus snow in the Sierra Nevada, California: Comparing Doppler profiling radar and surface observations of melting level, Journal of Hydrometeorology, 9, 194–211, https://doi.org/https://doi.org/10.1175/2007JHM853.1, 2008.

Marzano, F. S., Scaranari, D., Montopoli, M., and Vulpiani, G.: Supervised classification and estimation of hydrometeors from C-band dual-polarized radars: A Bayesian approach, IEEE transactions on Geoscience and Remote Sensing, 46, 85–98, https://doi.org/https://doi.org/10.1109/TGRS.2007.906476, 2007.

Mroz, K., Battaglia, A., Lang, T. J., Cecil, D. J., Tanelli, S., and Tridon, F.: Hail-detection algorithm for the GPM Core Observatory satellite sensors, Journal of Applied Meteorology and Climatology, 56, 1939–1957, https://doi.org/https://doi.org/10.1175/JAMC-D-16-0368.1, 2017.

Mroz, K., Battaglia, A., Lang, T. J., Tanelli, S., and Sacco, G. F.: Global precipitation measuring dual-frequency precipitation radar observations of hailstorm vertical structure: Current capabilities and drawbacks, Journal of Applied Meteorology and Climatology, 57, 2161–2178, https://doi.org/https://doi.org/10.1175/JAMC-D-18-0020.1, 2018.

Mroz, K., Battaglia, A., and Fridlind, A. M.: Enhancing consistency of microphysical properties of precipitation across the melting layer in dual-frequency precipitation radar data, Atmospheric Measurement Techniques, 17, 1577–1597, https://doi.org/https://doi.org/10.5194/amt-17-1577-2024, 2024.

Ortega, K. L., Krause, J. M., and Ryzhkov, A. V.: Polarimetric radar characteristics of melting hail. Part III: Validation of the algorithm for hail size discrimination, Journal of Applied Meteorology and Climatology, 55, 829–848, https://doi.org/https://doi.org/10.1175/JAMC-D-15-0203.1, 2016.

Park, H. S., Ryzhkov, A., Zrnić, D., and Kim, K.-E.: The hydrometeor classification algorithm for the polarimetric WSR-88D: Description and application to an MCS, Weather and forecasting, 24, 730–748, https://doi.org/https://doi.org/10.1175/2008WAF2222205.1, 2009.

Pejcic, V., Simmer, C., and Trömel, S.: Polarimetric radar-based methods for evaluation of hydrometeor mixtures in numerical weather prediction models, in: 2021 21st International Radar Symposium (IRS), pp. 1–10, IEEE, https://doi.org/https://doi.org/10.23919/IRS51887.2021.9466201, 2021.

Pejcic, V., Soderholm, J., Mühlbauer, K., Louf, V., and Trömel, S.: Five years calibrated observations from the University of Bonn X-band weather radar (BoXPol), Scientific Data, 9, 1–9, https://doi.org/https://doi.org/10.1038/s41597-022-01656-0, 2022.

Pippitt, J. L., Marks, D. A., and Wolff, D. B.: Dual polarimetric quality control for NASA's Global Precipitation Measurement (GPM) Mission Ground Validation program. 36th Conf. on Radar Meteorology, Breckenridge, CO, Amer. Meteor. Soc, in: 36th AMS Conference on Radar Meteorology, Breckenridge, CO, September, vol. 16, p. 2013, https://ams.confex.com/ams/36Radar/webprogram/Handout/Paper228522/36radarposter.pdf, 2013.

Planat, N., Gehring, J., Vignon, E., and Berne, A.: Identification of snowfall microphysical processes from Eulerian vertical gradients of polarimetric radar variables, Atmospheric Measurement Techniques, 14, 4543–4564, https://doi.org/10.5194/amt-14-4543-2021, 2021.

Protat, A., Louf, V., Soderholm, J., Brook, J., and Ponsonby, W.: Three-way calibration checks using ground-based, ship-based, and space-borne radars, Atmospheric Measurement Techniques, 15, 915–926, https://doi.org/https://doi.org/10.5194/amt-15-915-2022, 2022.

Reimann, L., Simmer, C., and Trömel, S.: Assimilation of 3D polarimetric microphysical retrievals in a convective-scale NWP system, Atmospheric Chemistry and Physics, 23, 14 219–14 237, https://doi.org/10.5194/acp-23-14219-2023, 2023.

Reuter, H. I., Nelson, A., and Jarvis, A.: An evaluation of void-filling interpolation methods for SRTM data, International Journal of Geographical Information Science, 21, 983–1008, https://doi.org/https://doi.org/10.1080/13658810601169899, 2007.

Ribaud, J.-F., Bousquet, O., Coquillat, S., Al-Sakka, H., Lambert, D., Ducrocq, V., and Fontaine, E.: Evaluation and application of hydrometeor classification algorithm outputs inferred from multi-frequency dual-polarimetric radar observations collected during HyMeX, Quarterly Journal of the Royal Meteorological Society, 142, 95–107, https://doi.org//10.1002/qj.2589, 2016.

Ribaud, J.-F., Machado, L. A. T., and Biscaro, T.: X-band dual-polarization radar-based hydrometeor classification for Brazilian tropical precipitation systems, Atmospheric Measurement Techniques, 12, 811–837, https://doi.org/10.5194/amt-12-811-2019, 2019.

Rysman, J.-F., Panegrossi, G., Sanò, P., Marra, A. C., Dietrich, S., Milani, L., and Kulie, M. S.: SLALOM: An all-surface snow water path retrieval algorithm for the GPM Microwave Imager, Remote Sensing, 10, 1278, https://doi.org/https://doi.org/10.3390/rs10081278, 2018.

Rysman, J.-F., Panegrossi, G., Sanò, P., Marra, A. C., Dietrich, S., Milani, L., Kulie, M. S., Casella, D., Camplani, A., Claud, C., et al.: Retrieving surface snowfall with the GPM microwave imager: A new module for the SLALOM algorithm, Geophysical Research Letters, 46, 13 593–13 601, https://doi.org/https://doi.org/10.1029/2019GL084576, 2019.

Ryzhkov, A. and Zrnic, D.: Precipitation and attenuation measurements at a 10-cm wavelength, Journal of Applied Meteorology and Climatology, 34, 2121–2134, https://doi.org/10.1175/1520-0450(1995)034<2120:PAAMAA>2.0.CO;2, 1995.

Ryzhkov, A. V. and Zrnic, D. S.: Radar polarimetry for weather observations, vol. 486, Springer, 2019.

Ryzhkov, A. V., Kumjian, M. R., Ganson, S. M., and Zhang, P.: Polarimetric radar characteristics of melting hail. Part II: Practical implications, Journal of Applied Meteorology and Climatology, 52, 2871–2886, https://doi.org/10.1175/JAMC-D-13-074.1, 2013.

Sanchez-Rivas, D. and Rico-Ramirez, M. A.: Calibration of radar differential reflectivity using quasi-vertical profiles, Atmospheric Measurement Techniques, 15, 503–520, https://doi.org/https://doi.org/10.5194/amt-15-503-2022, 2022.

Seiki, T.: Near-global three-dimensional hail signals detected by using GPM-DPR observations, Journal of the Meteorological Society of Japan. Ser. II, https://doi.org/https://doi.org/10.2151/jmsj.2021-018, 2021.

Shrestha, P., Mendrok, J., Pejcic, V., Trömel, S., Blahak, U., and Carlin, J. T.: Evaluation of the COSMO model (v5. 1) in polarimetric radar space–impact of uncertainties in model microphysics, retrievals and forward operators, Geoscientific Model Development, 15, 291–313, https://doi.org//10.5194/gmd-15-291-2022, 2022.

Stephens, G. L., Vane, D. G., Boain, R. J., Mace, G. G., Sassen, K., Wang, Z., Illingworth, A. J., O'connor, E. J., Rossow, W. B., Durden, S. L., et al.: The CloudSat mission and the A-Train: A new dimension of space-based observations of clouds and precipitation, Bulletin of the American Meteorological Society, 83, 1771–1790, https://doi.org/https://doi.org/10.1175/BAMS-83-12-1771, 2002.

Straka, J. M., Zrnić, D. S., and Ryzhkov, A. V.: Bulk hydrometeor classification and quantification using polarimetric radar data: Synthesis of relations, Journal of Applied Meteorology and Climatology, 39, 1341–1372, 2000.

Thompson, E. J., Rutledge, S. A., Dolan, B., Chandrasekar, V., and Cheong, B. L.: A dual-polarization radar hydrometeor classification algorithm for winter precipitation, Journal of Atmospheric and Oceanic Technology, 31, 1457–1481, https://doi.org//10.1175/JTECH-D-13-00119.1, 2014.

Tridon, F., Battaglia, A., Chase, R. J., Turk, F. J., Leinonen, J., Kneifel, S., Mroz, K., Finlon, J., Bansemer, A., Tanelli, S., et al.: The microphysics of stratiform precipitation during OLYMPEX: Compatibility between triple-frequency radar and airborne in situ observations, Journal of Geophysical Research: Atmospheres, 124, 8764–8792, https://doi.org//10.1029/2018JD029858, 2019.

Trömel, S., Ryzhkov, A. V., Bick, T., Mühlbauer, K., and Simmer, C.: Towards nowcasting of winter precipitation: The Black Ice Event in Berlin 2014, Meteorologische Zeitschrift, 26, 147–160, https://doi.org/10.1127/metz/2016/0778, 2017.

Trömel, S., Simmer, C., Blahak, U., Blanke, A., Ewald, F., Frech, M., Gergely, M., Hagen, M., Hörnig, S., Janjic, T., et al.: Overview: Fusion of radar polarimetry and numerical atmospheric modelling towards an improved understanding of cloud and precipitation processes, Atmospheric Chemistry and Physics Discussions, 2021, 1–36, https://doi.org/https://doi.org/10.5194/acp-21-17291-2021, 2021.

Trömel, S., Ryzhkov, A. V., Hickman, B., Mühlbauer, K., and Simmer, C.: Polarimetric Radar Variables in the Layers of Melting and Dendritic Growth at X Band—Implications for a Nowcasting Strategy in Stratiform Rain, Journal of Applied Meteorology and Climatology, 58, 2497 – 2522, https://doi.org/https://doi.org/10.1175/JAMC-D-19-0056.1, 2019.

Trömel, S., Blahak, U., Evaristo, R., Mendrok, J., Neef, L., Pejcic, V., Scharbach, T., Shrestha, P., and Simmer, C.: Fusion of radar polarimetry and atmospheric modeling, chap. Chapter 7, p. 293–344, https://doi.org/10.1049/SBRA557G_ch7, 2023.

van Lier-Walqui, M., Fridlind, A. M., Ackerman, A. S., Collis, S., Helmus, J., MacGorman, D. R., North, K., Kollias, P., and Posselt, D. J.: On polarimetric radar signatures of deep convection for model evaluation: Columns of specific differential phase observed during MC3E, Monthly weather review, 144, 737–758, https://doi.org/https://doi.org/10.1175/MWR-D-15-0100.1, 2016.

Vignon, E., Besic, N., Jullien, N., Gehring, J., and Berne, A.: Microphysics of snowfall over coastal East Antarctica simulated by Polar WRF and observed by radar, Journal of Geophysical Research: Atmospheres, 124, 11 452–11 476, https://doi.org//10.1029/2019JD031028, 2019.

von Terzi, L., Dias Neto, J., Ori, D., Myagkov, A., and Kneifel, S.: Ice microphysical processes in the dendritic growth layer: a statistical analysis combining multi-frequency and polarimetric Doppler cloud radar observations, Atmospheric Chemistry and Physics, 22, 11 795–11 821, https://doi.org/10.5194/acp-22-11795-2022, 2022.

Warren, R. A., Protat, A., Siems, S. T., Ramsay, H. A., Louf, V., Manton, M. J., and Kane, T. A.: Calibrating ground-based radars against TRMM and GPM, Journal of Atmospheric and Oceanic Technology, 35, 323–346, 2018.

Yang, J., Zhao, K., Zhang, G., Chen, G., Huang, H., and Chen, H.: A Bayesian hydrometeor classification algorithm for C-band polarimetric radar, Remote Sensing, 11, 1884, https://doi.org/https://doi.org/10.3390/rs11161884, 2019.

Zrnić, D. S., Ryzhkov, A., Straka, J., Liu, Y., and Vivekanandan, J.: Testing a procedure for automatic classification of hydrometeor types, Journal of Atmospheric and Oceanic Technology, 18, 892–913, https://doi.org//10.1175/1520-0426(2001)018<0892:TAPFAC>2.0.CO;2, 2001a.

Zrnić, D. S., Ryzhkov, A., Straka, J., Liu, Y., and Vivekanandan, J.: Testing a procedure for automatic classification of hydrometeor types, Journal of Atmospheric and Oceanic Technology, 18, 892–913, https://doi.org//10.1175/1520-0426(2001)018<0892:TAPFAC>2.0.CO;2, 2001b.